DENSITY FUNCTIONAL THEORY INVESTIGATION ON THICKNESS AND LOAD DEPENDENCY OF FRICTION FORCE BETWEEN GRAPHENE AND AU INTERFACES

A THESIS SUBMITTED TO
THE GRADUATE SCHOOL OF NATURAL AND APPLIED SCIENCES
OF
MIDDLE EAST TECHNICAL UNIVERSITY

BY

DUYGU GİZEM ŞENTÜRK

IN PARTIAL FULFILLMENT OF THE REQUIREMENTS
FOR
THE DEGREE OF MASTER OF SCIENCE
IN
PHYSICS

FEBRUARY 2018

Approval of the thesis:

DENSITY FUNCTIONAL THEORY INVESTIGATION ON THICKNESS AND LOAD DEPENDENCY OF FRICTION FORCE BETWEEN GRAPHENE AND AU INTERFACES

submitted by **DUYGU GİZEM ŞENTÜRK** in partial fulfillment of the requirements for the degree of **Master of Science in Physics Department, Middle East Technical University** by,

Prof. Dr. Gülbin DURAL ÜNVER
Dean, Graduate School of **Natural and Applied Sciences**

Prof. Dr. Altuğ ÖZPİNECİ
Head of Department, **Physics**

Assoc. Prof. Dr. Hande TOFFOLİ
Supervisor, **Physics Department, METU**

Examining Committee Members:

Prof. Dr. Oğuz GÜLSEREN
Physics Department, Bilkent University

Assoc. Prof. Dr. Hande TOFFOLİ
Physics Department, METU

Prof. Dr. Çiğdem ERÇELEBİ
Physics Department, METU

Assoc. Prof. Dr. Emre TAŞCI
Physics Engineering Department, Hacettepe University

Prof. Dr. Hamit YURTSEVEN
Physics Department, METU

Date:

I hereby declare that all information in this document has been obtained and presented in accordance with academic rules and ethical conduct. I also declare that, as required by these rules and conduct, I have fully cited and referenced all material and results that are not original to this work.

Name, Last Name: DUYGU GİZEM ŞENTÜRK

Signature :

ABSTRACT

DENSITY FUNCTIONAL THEORY INVESTIGATION ON THICKNESS AND LOAD DEPENDENCY OF FRICTION FORCE BETWEEN GRAPHENE AND AU INTERFACES

ŞENTÜRK, DUYGU GİZEM
M.S., Department of Physics
Supervisor : Assoc. Prof. Dr. Hande TOFFOLİ

February 2018, 76 pages

As the investigation of materials at nano scale become possible with today's technology it is observed that some physical phenomenons have different characteristics at atomistic scale than macroscopic one because of the quantum mechanical effects. One of these physical processes that differs at nano scale is the friction force. While it is expected that the friction force to be independent of contact area and velocity according to Amontos-Coulomb laws, it was observed that it changes by the effect of some parameters such as contact area, velocity, load and temperature at smaller scales. This study will include nanotribological calculations which analyzes the friction force between objects at atomic level.

The lateral friction force that arises from the relative sliding motion of materials can be investigated in experimental manner using the Friction Force Microscopy (FFM) which is modified version of the Atomic Force Microscopy (AFM). It is also possible to obtain a detailed understanding of friction in atomic scale by modelling the mechanism of FFM using computational methods. The ab initio Density Functional Theory (DFT) is one of these methods that one can perform accurate calculations for the relative sliding motion of FFM probe tip and the surface. The importance of these kind of numerical methods is the convenience of investigating the wide range of material interactions that are not achievable with experimental methods.

As it was observed that the two dimensional materials such as graphene, hexagonal boron nitride(h-BN) , MoS_2 provides good performance as dry lubricants, the scope of the nanotribology studies shifted into the frictional behaviors of these systems and their effects on other type of materials. In this thesis, we focus on the lateral friction force between two dimensional graphene sheets and three high-symmetry surfaces of gold. Our aim is to understand the results of FFM experiments by modelling the friction mechanism between Au coated probe-tip and graphene surface by implementing static calculations based on Density Functional Theory. As the Au coated probe slides over graphene, Au surfaces with different orientations would interact with graphene surface and three of them namely Au(100), Au(110) and Au(111) are reviewed as the subjects of this study. The effects of physical variables such as an external load applied to structures and increasing the thickness of the surfaces were interpreted.

Results of this thesis can provide useful informations about minimizing the friction between objects with the help of different parameters which would be beneficial in industrial manner about reducing the loss of energy arises due to friction.

Keywords: Computational Physics, Density Functional Theory, friction, graphene, gold

ÖZ

GRAFEN VE AU ARAYÜZLERİ ARASINDAKİ SÜRTÜNME KUVVETİNİN KATMAN SAYISI VE YÜKE BAĞLI DEĞİŞİMİNİN YÜK YOĞUNLUĞU FONKSİYONELİ TEORİSİ İLE İNCELENMESİ

ŞENTÜRK, DUYGU GİZEM
Yüksek Lisans, Fizik Bölümü
Tez Yöneticisi : Doç. Dr. Hande TOFFOLİ

Şubat 2018 , 76 sayfa

Günümüzün gelişen teknolojisinin materyallerin nano boyutlarda incelenmesini mümkün kılmasıyla, atomistik boyutlarda önem kazanan kuantum mekaniksel etkilerin sürece dahil olmasıyla birlikte makro ölçektekinden daha farklı işleyen fiziksel süreçler araştırılabilmeye başlamıştır. Bahsi geçen değişikliklerden biri de sürtünme kuvveti üzerinde gözlemlenmiştir. Örneğin; Amontons-Coulomb kanunlarına göre temas alanı ve hareket hızından bağımsız olması beklenen sürtünme kuvveti daha küçük ölçeklerde, temas alanı, yük, hız ve sıcaklık gibi parametrelere bağlı olarak değişmektedir. Bizim çalışmamız da nano boyutlardaki sürtünme kuvvetini inceleyen nanotriboloji hesaplarını kapsayacaktır.

Malzemeler arasındaki yanal manipulasyona bağlı sürtünme davranışı deneysel anlamda Atom Kuvvet Mikroskobu(AKM) prensibine dayanan Sürtünme Kuvveti Mikroskobu(SKM) kullanılarak araştırılabilmektedir. Teorik anlamda sürtünme yapısının Yük Yoğunluğu Fonksiyoneli Teorisi(DFT) aracılığıyla atomik düzeyde incelenmesinin mümkün kılınması ise hem incelenebilen materyal çeşidi konusunda sağladığı esneklik hem de deneysel açıdan test edilmesi zor olan sistemlerin araştırılabilmesini kolaylaştırması sebebiyle nanotriboloji çalışmaları konusunda nümerik uygulamaların önemini artırmıştır.

Grafen, hegzagonal boron nitrat(h-BN), MoS_2 gibi iki boyutlu malzemeler, sahip oldukları güçlü elektronik, mekanik ve optik özellikler sayesinde katı kayganlaştırıcılar olarak iyi bir performans gösterdiklerinin keşfedilmesiyle nanotriboloji alanında en çok dikkat çeken ve araştırılan materyallerden olmuşlardır. Çalışmamızda metal kaplı iğne ucu ile iki boyutlu yüzey arasındaki yanal manipülasyona bağlı sürtünme kuvvetini ölçen bir SKM'nin nümerik olarak modellenmesi hedeflenmiştir. Bu amaçla yüzey merkezli kübik kristal(FCC) bir yapıya sahip olan altın(Au) materyalinin Au(100), Au(110) ve Au(111) gösterimleriyle tanımlanan yüksek simetri arayüz konfigürasyonları ve tek katmanlı grafen yüzeyi arasındaki etkileşim DFT hesaplamaları ile ele alınmıştır. Hesaplamalarımızda öncelikle yüzeyler arasındaki zayıf van der Waals etkileşimlerini en iyi tanımlayan değiş-tokuş fonksiyonellerinin belirlenmesini takriben bahsi geçen altın yüzeyleri ve tek katmanlı grafen yüzeyi birbiri üzerinde tek yönde paralel olarak kaydırılarak elde edilecek yanal sürtünme kuvveti ve sonrasında bu kuvvetin yüzeye dik olarak uygulanacak bir kuvvete bağlılığı incelenmiştir.

Bu tezden elde edilecek sonuçlara göre sürtünme kuvvetinin hangi yüzey etkileşimlerinde daha düşük olduğu ve kullanılan parametrelerin sürtünme davranışını hangi boyutta azaltabileceği anlaşılabilecek ve bu bilgiler endüstriyel anlamda sürtünme etkisiyle kaybedilen enerji miktarının azaltılması amacıyla kullanılabilecektir.

Anahtar Kelimeler: Hesaplamalı Fizik, Yük Yoğunluğu Fonksiyoneli Teorisi, sürtünme, grafen, altın

To my aunt, ***Miyase Höke***

ACKNOWLEDGMENTS

I would first like to express my deepest gratitude to my advisor Assoc. Prof. Dr. Hande Toffoli for being such an inspiring mentor for me with her patience, support and encouragement. I am grateful to her for the guidance and the motivation that makes possible this study to be materialized. I also want to thank Assoc. Prof. Dr. Emre Taşcı for his guidance and support since my undergraduate senior year. I am lucky to meet such excellent tutors at the beginning of my research career.

I owe a very important debt to my family Miyase Höke, Sultan Höke and Mehmet Yücel Şentürk who were always there for me with their endless love and support. Without them none of the things I have achieved would have been possible.

I also thank the members of office:334, Gözdenur Toraman, Ozan Dernek and Fırat Yalçın for their insightful comments and being such good friends. I will always miss the times we share this office. And special thanks goes to my dearest Kutay for his patience, suggestions and help during these stressful times and making my life better with his existence.

This work is financially supported by TÜBİTAK (The Science and Technological Research Council of Turkey).(Grant no:115F493)

TABLE OF CONTENTS

ABSTRACT v

ÖZ vii

ACKNOWLEDGMENTS x

TABLE OF CONTENTS xi

LIST OF TABLES xiv

LIST OF FIGURES xv

CHAPTERS

1 INTRODUCTION 1

1.1 The History of Tribology 3

1.2 Theoretical Models for Friction 4

1.3 Literature Review 8

1.4 Outline 10

2 DENSITY FUNCTIONAL THEORY 13

2.1 Many Body Schrödinger Equation 13

2.2 The Total Energy 16

2.3 Exchange-Correlation Functionals 19

2.4 Hohenberg-Kohn Theorem 20

2.5 The Kohn-Sham Equations 21

2.6 The Plane Wave Basis and The Pseudopotentials 22

2.7 The van der Waals Interaction 24

2.8 Calculation Details 26

  2.8.1 Structure Optimization 27

  2.8.2 The Calculation of the Friction Force 28

3 GRAPHENE-GRAPHENE INTERACTION 31

3.1 Graphene Lattice Constant and Separation Distance 31

3.2 Potential Energy Surface 35

3.3 Dependence of the Friction Force on the Number of Layers in Graphene Interfaces 38

3.4 Load Dependency of Friction Force Between Graphene Surfaces 40

4 AU INTERFACE-GRAPHENE INTERACTION 45

4.1 Au Bulk Structure 45

4.2 Low-index Surfaces of Au 46

4.3 Graphene on Au interface 50

  4.3.1 Geometry Optimization 50

  4.3.2 Equilibrium Separation Distance 55

  4.3.3 Load Dependence of Energy and Friction Force . . 57

    4.3.3.1 Au(100) Interface 58

4.3.3.2 Au(110) Interface 61

4.3.3.3 Au(111) Interface 64

5 CONCLUSION 69

REFERENCES 73

LIST OF TABLES

TABLES

Table 3.1 Comparison of experimental and numerically calculated lattice constant of monolayer graphene with different pseudopotentials and calculation errors 33

Table 3.2 Graphene C-C bond length and equilibrium separation of graphene layers with different vdW protocols. Experimental and previously calculated theoretical values are also included for comparison 35

Table 3.3 Average friction force along x-direction with applied vertical contact force for bilayer graphene 41

Table 3.4 Average friction force of trilayer graphene system along x-direction with applied vertical contact force 44

Table 4.1 Percentage error for adjustment of Au(100) and graphene surface unit cells 51

Table 4.2 Percentage error for adjustment of Au(110) and graphene surface unit cells 53

Table 4.3 Percentage error for adjustment of Au(111) and graphene surface unit cells 54

Table 4.4 Equilibrium separation distance and interaction energy between graphene and Au(111), Au(110), Au(100) interfaces 56

Table 4.5 Average friction force between Au(100) and graphene monolayer along x-direction with applied vertical contact force 59

Table 4.6 Average friction force between Au(110) and graphene monolayer along x-direction with applied vertical contact force 63

Table 4.7 Average friction force between Au(111) and graphene monolayer along x-direction with applied vertical contact force 66

LIST OF FIGURES

FIGURES

Figure 1.1 Prandtl-Tomlinson model: A point mass dragged in a periodic potential. 5

Figure 1.2 Characteristic of motion with respect to spring stiffness. Source [1] 6

Figure 1.3 Friction force hysteresis along position of particle at F_N=0.65 [nN] and v_0=25 [nm/s]. Taken from [2] 6

Figure 1.4 Displacement between spring and tip positions dependent to variation in velocity and stiffness 8

Figure 2.1 Kohn-Sham self-consistency cycle 23

Figure 2.2 Pseudopotential and pseudowave function with respect to real system 24

Figure 3.1 Total energy [eV/C-atom] vs lattice constant [$\mathring{A}$] with (a)PBE (b)PW91 (c)PZ pseudopotentials 32

Figure 3.2 AB-stacked bilayer graphene (a)top view (b) side view 33

Figure 3.3 Graphene (a)C-C bond length evaluated by DFT-D, vdW-DF and vdW-DF2-C09 functionals and (b)layer separation with vdW-DF2-C09 functional 34

Figure 3.4 PES configuration with (a)DFT-D and (b)vdW-DF2-C09 functionals 36

Figure 3.5 Lateral displacement along the x-direction of the upper graphene layer separated by equilibrium interlayer distance while the bottom layer kept fixed 37

Figure 3.6 Lateral energy and friction force for bilayer graphene at different degrees of freedom 38

Figure 3.7 Lateral energy variation with respect to layer number for (a) bilayer graphene and (b) trilayer graphene 39

Figure 3.8 Friction force variation with respect to number of layer for (a) bilayer graphene and (b) trilayer graphene 40

Figure 3.9 Load vs separation distance for bilayer graphene 41

Figure 3.10 Load dependency of (a)lateral energy and (b)friction force trend (c)average friction (d)friction coefficient for bilayer graphene 42

Figure 3.11 (a)Friction force trend and load dependency of (a)average friction and (b)friction coefficient along lateral displacement for trilayer graphene . 43

Figure 4.1 Total energy [Ry] vs lattice constant [$\mathring{A}$] of bulk Au 46

Figure 4.2 Low index (a)100, (b)110, (c)111 surfaces of fcc Au crystal 47

Figure 4.3 Au(100) surface at (a)on top and (b)side view with ABAB stacking 48

Figure 4.4 Au(110) surface on top view with ABAB stacking 48

Figure 4.5 Au(111) surface on top view of ABC stacking 49

Figure 4.6 Graphene and ABA stacked Au(100) unit cell configuration (a)on top and (b)side view 51

Figure 4.7 Graphene and ABA stacked Au(110) unit cell configuration (a)on top and (b)side view 53

Figure 4.8 Graphene and ABCAB stacked Au(111) unit cell configuration (a)on top and (b)side view 54

Figure 4.9 Equilibrium separation distance for (a)Au(100), (b)Au(110) and (c)Au(111) surfaces and graphene monolayer 56

Figure 4.10 Lateral displacement sites of graphene over Au(110) interface . . . 57

Figure 4.11 (a) Interaction energy (b)lateral friction force of vertically loaded Au(100)-graphene structure in several orders 58

Figure 4.12 (a) Average lateral friction force (b)friction coefficient with increasing applied load over graphene-Au(100) interface configuration . . . 60

Figure 4.13 (a) Average charge density of stick-slip sites of graphene-Au(100) interface configuration under (a) 0 nN/C-atom (b) 0.005 nN/C-atom normal force 60

Figure 4.14 (a) Interaction energy (b) lateral friction force of vertically loaded Au(110)-graphene structure in several order of magnitudes 62

Figure 4.15 (a) Average lateral friction force (b)friction coefficient with increasing applied load over graphene-Au(110) interface configuration . . . 63

Figure 4.16 (a) Average charge density of stick-slip sites of graphene-Au(110) interface configuration under (a) 0 nN/C-atom (b) 0.019 nN/C-atom normal force 64

Figure 4.17 (a),(c) Interaction energy and (b),(d) lateral friction force of vertically loaded Au(111)-graphene structure in several order of magnitudes . . 65

Figure 4.18 (a) Average lateral friction force (b)friction coefficient with increasing applied load over graphene-Au(111) interface configuration . . . 66

Figure 4.19 (a) Average charge density of stick-slip sites of graphene-Au(111) interface configuration under (a) 0 nN/C-atom (b) 0.005 nN/C-atom normal force 67

CHAPTER 1

INTRODUCTION

Even though we may not pay attention to it in our everyday lives, friction is one of the most significant physical phenomenon that is essential for daily life because of making some fundamental actions possible such as walking. It also plays a crucial role in modern machinery where driving wheels, brackets in car engines are some of the productive examples of friction. On the other hand the energy dissipation arising due to friction force, in other words the physical resistance between bodies comes out as a problem that one has to overcome in industrial manner because of its economical impacts. Although friction has a great influence in nature with both its benefits and disadvantages there is still no clear explanation about the physical processes behind it.

In order to explain the detailed mechanism underlying the macroscopic and microscopic scale friction and the properties that governs the physical resistance, "tribology" has emerged as a popular research field in recent years due to the improvements in technology. This term is derived from a Greek word "*tribos*" that means rubbing and its first usage is in the Jost Report(1966) which is a study conducted to investigate the wasted financial resources because of the friction [3]. Tribology includes all researches on not only the process of friction but also wear and lubrication that can be applied to various areas from aircrafts to mechanical interactions between biological parts.

The experimental investigation of friction at the atomic scale has been made possible by the development of a new technique referred to as Friction Force Microscopy (FFM), which is a modified version of the conventional Atomic Force Microscopy

(AFM) technique. As the first investigations of atomic scale friction performed by FFM technique in 1987 [4] revealed the atomic stick-slip motion of sliding surfaces, the focus of tribology studies changed from macro scales to atomic scales and this new field came to be called "nanotribology". Since the surface areas of the bodies in contact consist of several small asperities at micro and nano scales even though they seem perfectly smooth to the naked eye, the real surface area one should consider is larger than the area presumed at the macro level. The main idea behind the instruments is measuring the friction between a surface and the probe tip which represents a single asperity [5].

A large body of theoretical work has been constructed over the years in order to explain the characteristic of friction. One dimensional Prandtl-Tomlinson (PT) [6],[7] and Frenkel-Kontorova-Tomlinson (FK) [8] models are the simplest and most commonly used approaches in this field that describe the physical process of friction. While these models successfully represent the certain superficial properties of friction, the actual mechanisms are much more complex. Therefore, nanotribology is an intriguing subject also for computational scientist where several methods can be employed to obtain a detailed understanding of this physical phenomena by modelling the mechanism of FFM in wide range of material interactions. The Density Functional Theory (DFT) is one of these methods that one can perform very accurate static calculations for the relative sliding motion of FFM probe tip and the surface. Fitting the outcomes to PT or FK models makes possible to acquire a detailed description of both the stick-slip characteristic of motion and the energy dissipation arising through the interaction between materials.

In this thesis we aim to make a contribution to the understanding of tribology at the nanoscale by investigating the manipulation of lateral friction force between two dimensional materials and metal surfaces using graphene and different low-dimensional gold surfaces. Density Functional Theory is employed to obtain the characteristics of materials and their interactions during lateral motion of monolayer graphene on Au interfaces. The effects of physical variables such as an external load applied to structures and increasing the thickness of the surfaces were studied in accordance with the mentioned friction models.

1.1 The History of Tribology

Throughout the history from ancient times to recent days friction has attracted the attention of people where creating fire by rubbing branches together can be thought of as an example of one of the first innovations of humankind from a tribological point of view. The awareness of friction that technology was invented by using it or against it by the first people, became a scientific thought where formulations and ideas of dissipation were enhanced in following eras [9].

The earliest formal treatment of tribology were performed by Leonardo Da Vinci (1452-1519) where his studies include the friction on inclined and horizontal planes and low-friction bearings. He demonstrated that friction is linearly proportional to applied normal load (F_N) but independent of the contact area size [10] and introduced the friction coefficient as proportionality between the friction force (F_f) to normal load. Another scientist named Guillaume Amontons (1663-1705) also investigated the nature of macroscale friction and deduced the same observations with Da Vinci more than hundred years later. Since Da Vinci's observations had not been published, these two fundamental principle of macroscale friction is known as the "Amontons' Laws of Friction" [11]. In the eighteenth century, mathematician Leonard Euler(1707-1783) emphasized the difference between the static and kinetic friction. Charles Augustin de Coulomb (1736-1806) contributed a third principle based on his experiments achieved in different environmental conditions that the friction force is independent from the sliding velocity of contacts[12]. Finally the three fundamental laws of friction in macroscale are:

- **Amontons' first law**: Friction is independent from the area size of the contacting bodies.
- **Amontons' second law**: Friction is directly proportional to the applied normal load.
- **Coulomb's law**: Friction is independent from the relative sliding velocity of bodies.

Following that, Isaac Newton (1642-1727) formulated these three principles and introduced the friction coefficient as ratio of friction force to normal load as

$$F_f = F_n \mu \tag{1.1}$$

Here in Eq. 1.1 static friction can also been demonstrated which is the maximum value that had to be reached in order to system start sliding lateral motion. In addition to these laws, it was later observed that the actual area of the rough surfaces consisting of multiple nanoscale asperities is different than apparent contact area and friction force was reformulated by Bowden and Tabor as

$$F_f = \tau \sum A_{asp} \tag{1.2}$$

where τ is effective shear strength between surfaces and A_{asp} represents the area of each small asperity [13]. Even with the increased sophistication, all these models remain to be inadequate for explaining the origins of friction at the microscopic level. A better understanding of friction requires detailed theoretical modelling as discussed in the next subsection.

1.2 Theoretical Models for Friction

The Prandtl-Tomlinson (PT) model rationalizes the Stokes and Coulomb approximations regarding the force resisting motion. While Stokes claims that the drag force linear in the relative velocity between solid and fluid, according to Coulomb the kinetic friction F_k is independent of velocity [14].

The PT model can be considered as the basis for dry friction and is used to explain the effect of such parameters as the plasticity, elastic constants, velocity and friction. However, there is a deficiency in the model since the change in the surface potential due to wear is ignored. This deficiency can be eliminated by taking into account plastic deformation. This model that is proposed at 1928, contains both the motion of

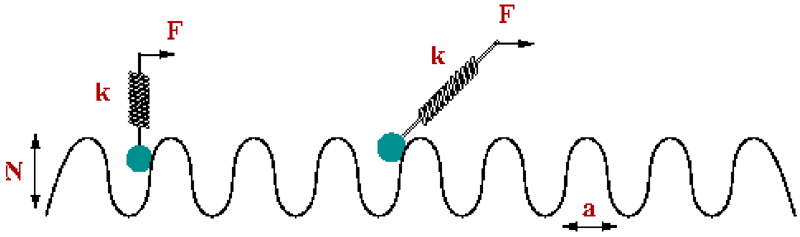

Figure 1.1: Prandtl-Tomlinson model: A point mass dragged in a periodic potential.

the point mass in a periodic potential and the influence of thermal fluctuations which leads to a logarithmic dependency of frictional force on the velocity. The PT model can also be thought of as an independent oscillator model which describes the motion of a point particle of mass m, dragged through a potential landscape with velocity v_0 as illustrated at Figure 1.1 [15]. The spring corresponds to the elastic coupling of a surface to the point particle where the point particle represents an atom. The general equation of motion for this model

$$m\ddot{x} = k(v_0 t - x) - \eta\dot{x} - N\sin\left(2\pi x/a\right) \tag{1.3}$$

where x is the position of the point particle with mass m, η is the damping factor, k is the stiffness of the pulling spring, N is the amplitude of the periodic potential and a is the spatial period of the potential. The motion of the point mass considered as it follows a non-continuous path with stick-slip behaviour when the spring is assumed soft enough. In the case of a soft spring, the spring force F becomes constant over one or several periods.

One of the fundamental outcomes Prandtl proposes with this representation is the relation between static and dynamic friction where the maximum value of the lateral force that the body experiences before starting to move should be equal to the maximum value of static friction. In terms of the spring model this static well is derived proportional to critical spring stiffness as $F = N sin k_c x$. The characteristic of the motion of point mass at the end of the spring can be demonstrated as follows. In the case of $k_s < k_c$ stick-slip behaviour occurs with sudden jumps with respect to the magnitude of the ratio of critical stiffness k_c and spring stiffness k_s and if $k_s > k_c$ particle achieves a continuous movement along sinusoidal path. The energy landscape

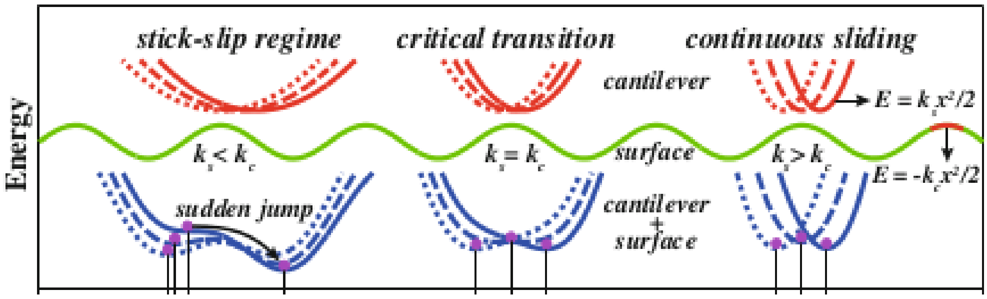
stick-slip regime
critical transition
continuous sliding
cantilever
$E = k_s x^2/2$
Energy
$k_s < k_c$
$k_s = k_c$
surface
$k_s > k_c$
$E = -k_c x^2/2$
sudden jump
cantilever + surface

Figure 1.2: Characteristic of motion with respect to spring stiffness. Source [1]

of the motion is as illustrated at Figure 1.2

The sliding particle starts out stuck at a certain position at the edge of potential well designated by U(x) until the force applied by the spring exceeds the maximum static friction force at which point particle suddenly slips over the potential barrier. During the stick phase of the particle, friction force builds up while it reduces as slipping occurs [16]. One example to clarify the variation of friction force during atomic stick-slip behaviour, the friction loop during sliding of NaCl(100) surface forward and backward is presented at Figure 1.3.

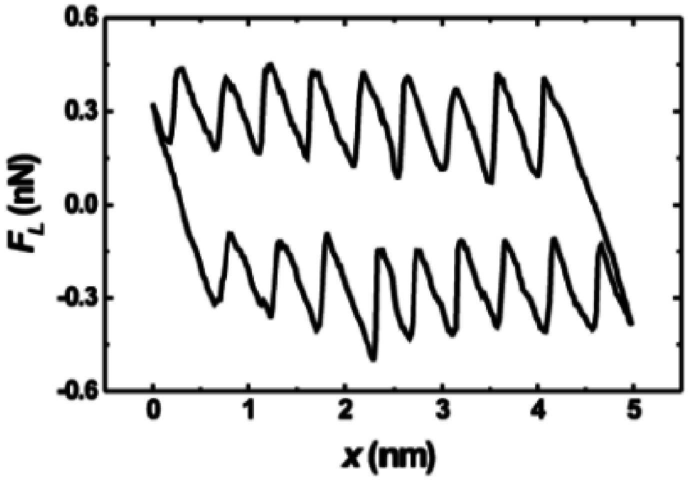

Figure 1.3: Friction force hysteresis along position of particle at F_N=0.65 [nN] and v_0=25 [nm/s]. Taken from [2]

The saw-tooth like picture of friction force as a function of relative position of mass at Figure 1.3 shows the sign changes along forward and backward lateral forces F_L. If the system experiences the continuous sliding, the saw-tooth picture of friction turns into a smoother variation. Average value of the lateral forces that corresponds to average amount of energy dissipated per scanning distance, determines the friction force of system [16].

$$F_x = \langle F_l \rangle \tag{1.4}$$

In tribology experiments using FFM such as the one conducted by Bouhacina et al., it was observed that the friction has a logarithmic dependency on velocity [17] at finite temperature. Until this point, PT model was described at zero temperature. The mechanism of the PT model states that, after the critical force is reached at stick-slip motion, mass jumps through one potential minimum to another and even if the applied force is reduced, the body continues its motion under the effect of the initially applied force. However, when temperature is included in the considered system, the body can jump over the potential energy barrier without any external force but just due to the thermal activation. The dependence of friction to velocity related to thermal activity is expressed as

$$v \approx C e^{-U_0/k_B T} \frac{Fa}{k_B T} \tag{1.5}$$

where F is the spring force, U_0 is the periodic potential with period a, k_B Boltzmann constant and T is the absolute temperature [15].

The phase-space illustration for effects of both change in velocity and spring stiffness on relative motion of spring and tip is shown at Figure 1.4 where the x axis corresponds to stiffness and y-axis is the increasing velocity of the spring while spring is always in front of the point mass. Whereas the influence of velocity on the difference between the location of point mass x_m and the other end of the spring X_s is relatively low, it is larger for soft springs. For the lateral force $F_l = k_s(X_s - x_m)$, the more lubricant case would be observed with increasing stiffness of the spring that can be called spring-free condition.

In addition to stiffness and velocity, external applied load also affects the value of the friction force. The increasing normal load leads to a higher interaction with increasing

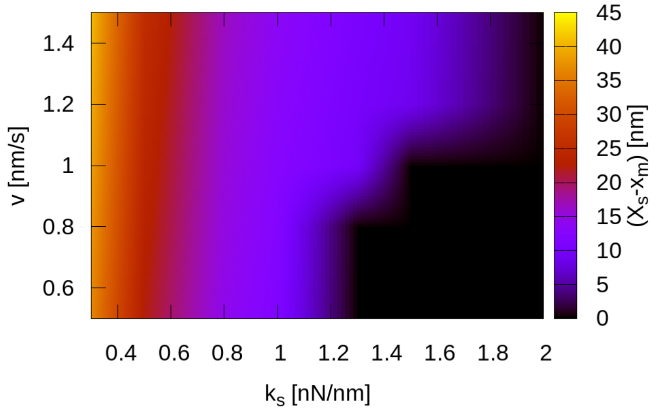

Figure 1.4: Displacement between spring and tip positions dependent to variation in velocity and stiffness

contact area of the bodies and thus higher potential energy barrier would occur for the mass jump over. This result, which follows from the PT model is consistent with macroscopic friction laws.

It is possible to extend this one-dimensional model to sliding bodies represented by many independent atoms coupled by springs with different stiffness. This is the so-called Frenkel-Kontorova (FK) model which is more realistic than PT model to express the interaction between relative sliding surfaces.

The dependencies of the friction force on the stiffness, normal load, velocity and temperature have been investigated both theoretically and experimentally. A brief summary of the previous studies in literature that investigated the load and thickness dependency of friction will be presented next in accordance with the scope of our study.

1.3 Literature Review

First-principles quantum mechanical materials modelling methods such as Density Functional Theory (DFT) has emerged as a powerful tool in nanotribology studies. One of the earliest atomic scale friction studies using DFT was conducted by Zhong et. al. [18] which was also used as an instructive study for our research. In this work, friction between Pd atoms and graphite under external load was investigated and it was observed that the friction coefficient increased with applied load in agreement with the AFM studies.

It is later observed that graphene, produced by cleaving graphite, has superior friction behaviour that makes it a good candidate as a lubricant. In the contrast to three dimensional materials where the lower friction is obtained at high stiffness, graphene leads lower friction when it is in flexible form. One of the studies investigating the properties of graphene such as the AFM study conducted by Lee et al. [19] revealed that friction increases as the number of graphene layers stacked decreases, which is related to the higher stiffness of the thin layered systems [20]. This experimental observation was supported by *ab initio* DFT studies such as the one performed by Righi et. al. [21] presented the PES corrugation by including the effect of van der Waals (vdW) interactions and concluded that when graphene layers are tightly bound to the substrate, both the vertical and lateral stiffness decreases as the number of layers increases. Following these studies that focused on the nanotribological properties of graphene, the investigations about the influence of graphene on other types of materials were conducted. One of these studies presented by Cahanagirov et. al [22] stated that inserting bilayer graphene between two Ni(111) interfaces leads to lower friction than monolayer graphene-Ni(111) coupling. The load carrying capacity of graphene was also one of the intriguing subjects to investigate. The AFM experiments of Filleter et. al. on single and bilayer graphene sheets grown on SiC suggest that there is a linear proportionality between load and friction force for graphene[23]. In addition, studies utilizing Molecular Dynamics(MD) suggest that in the low-load regime graphene increases the load carrying capacity of surfaces such as presented in the study of Klemenz et. al. [24] where the frictional behaviour of Pt(111) surface with and without graphene wear was discussed.

Other two dimensional materials namely MoS_2, fluorographene and WO_2 have also been considered as promising lubricants. Cahangirov et. al [25] observed that these materials show low stiffness even in high loads where the materials avoid stick-slip sliding and follows a continuous sliding path when they reach the critical stiffness. This study performed by *ab initio* calculation methods was achieved based on Prandtl-

Tomlinson model and friction force and stiffness of the materials as a function of external load was calculated. The results are consistent with the friction calculations of Zhong mentioned above. The MoS_2-graphene interface also shows remarkable superlubricity properties. The study conducted by Wang et. al. [26] proposed that the key reason behind the potential energy corrugation and friction in the atomic scale is the interlayer charge density fluctuation instead of the average charge density or adhesion energy.

The load dependency of metallic surfaces was also investigated with the DFT method. One of these studies is the one conducted on the dry and wearless Cu(111) interface by Wolloch et. al. [27] reveals that there is an exponential increase in friction force proportional to applied load. This result is consistent with the experimental study of Gosvami et al. [28] observed for Au(111) and Cu(100) interface that there is a strong increase in friction at high loads.

1.4 Outline

In this thesis, we focus on the lateral friction force between two dimensional graphene sheets and three high-symmetry surfaces of gold. Our aim is to understand the results of FFM experiments by modelling the friction mechanism between Au coated probe-tip and graphene surface by implementing static calculations based on Density Functional Theory. As the Au coated probe slides over graphene, Au surfaces with different orientations would interact with graphene surface and three of them namely Au(100), Au(110) and Au(111) are reviewed as the subjects of this thesis. In order to determine the variation in energy and lateral friction force along zigzag orientation on the x-y plane, interaction between Au interface and graphene monolayer was calculated one-by-one for each position during the lateral motion of graphene. The results we obtained were analysed and the effect of applied normal load and thickness of surfaces were investigated.

This thesis consists of five parts. In Chapter 2 a brief explanation for Density Functional Theory is presented. The procedure of calculations including the chosen parameters and how DFT is applied to this kind of dynamical systems with van der

Waals interaction is justified. Chapter 3 contains the study on graphene-graphene interaction which is performed as a benchmark study in order to determine the proper procedure and parameters of friction analyses. Both the number of layer and load dependency of friction between graphene layers are presented. Chapter 4 includes the outcomes of graphene-Au interactions in a comparative representation by determining the external effects to manipulate the friction force between different oriented interfaces. In Chapter 5 a discussion and the summary of all results we obtained is provided.

CHAPTER 2

DENSITY FUNCTIONAL THEORY

Thanks to rapid developments in computational techniques and computer power theoretical prediction of materials properties at the atomic scale possible. Density Functional Theory (DFT) is regarded as the state-of-the-art *ab initio* approach for materials modelling where it provides accurate information for a large scale of fields from biological sciences to mineralogy. The main idea behind DFT is shifting the focus from the unattainable many-particle wavefunction to the electronic charge density. This conversion proposes a much simpler mathematical solution by decreasing the number of variables. In this chapter, we outline the basic ideas behind DFT and present the approximations that have been developed to make this method practically viable.

2.1 Many Body Schrödinger Equation

The ground and excited states can, in principle, be obtained by means of solving the many-particle Schrödinger equation for the wavefunction Ψ. The time-independent form of Shrödinger equation is

$$(-\frac{\hbar^2}{2m}\nabla^2 + V)\Psi = E\Psi \tag{2.1}$$

Here the sum of kinetic and potential energies in parenthesis at left hand side of the Eq. 2.1 is called the Hamiltonian operator ($\hat{H}$). The Hamiltonian consists of the interactions of N_n nuclei and N_e electrons as follows

$$\begin{aligned}\hat{H} =& \frac{-\hbar^2}{2m_e}\sum_{i}^{N_e}\nabla_i^2 - \frac{\hbar^2}{2M_I}\sum_{I}^{N_n}\nabla_I^2 + \frac{1}{2}\frac{e^2}{4\pi\epsilon_0}\sum_{i\neq j}^{N_e}\frac{1}{|\vec{r}_i - \vec{r}_j|} \\ &+ \frac{1}{2}\frac{e^2}{4\pi\epsilon_0}\sum_{I\neq J}^{N_n}\frac{Z_I Z_J}{|\vec{R}_I - \vec{R}_J|} - \frac{e^2}{4\pi\epsilon_0}\sum_{i,I}^{N_e,N_n}\frac{Z_I}{|\vec{r}_i - \vec{R}_I|}\end{aligned} \tag{2.2}$$

The terms on the right hand side of the Eq. 2.2 are the electronic and nuclear kinetic energies, repulsive Coulomb interaction between electrons and between nuclei and finally the attractive interaction between electrons and nuclei, respectively. $\vec{R}_I$ is the position of I^{th} nucleus and $\vec{R}_i$ is the i^{th} electron's position where m_e and M_I are mass of electron and nucleus. For convenience atomic units are used for $\hat{H}$ representation rather than SI units by employing the Hartree energy in Eq. 2.4 and Bohr radius terms in Eq. 2.3.

$$a_0 = \frac{4\pi\epsilon_0\hbar^2}{m_e e^2} \tag{2.3}$$

$$E_H = \frac{\hbar^2}{m_e a_0^2} = \frac{e^2}{4\pi\epsilon_0} \tag{2.4}$$

Then the Hamiltonian in terms of atomic units becomes

$$\begin{aligned}\hat{H} &= -\sum_i \frac{\nabla_i^2}{2} - \sum_I \frac{\nabla_I^2}{2M_I} - \sum_{i,I}\frac{Z_I}{|\vec{r}_i - \vec{R}_I|} + \frac{1}{2}\sum_{i\neq j}\frac{1}{|\vec{r}_i - \vec{r}_j|} + \frac{1}{2}\sum_{I\neq J}^{N_n}\frac{Z_I Z_J}{|\vec{R}_I - \vec{R}_J|} \\ &= \hat{T}_e + \hat{T}_n + \hat{V}_{en} + \hat{V}_{ee} + \hat{V}_{nn}\end{aligned} \tag{2.5}$$

It is known that nuclei are heavier than electrons and they move much slowly where electrons change positions with respect to nuclei. In order to reduce the complexity of interaction, Born and Oppenheimer proposed an approximation which assumes that the motion of electrons and nuclei independent which means that the Hamiltonian operators corresponding to the two species can be written independently. Using this approximation the electronic Hamiltonian can be written in the much simpler form [29]:

$$\hat{H} = -\sum_i \frac{\nabla_i^2}{2} + \sum_i \hat{V}_{en}(\vec{r}_i) + \frac{1}{2}\sum_{i \neq j} \frac{1}{|\vec{r}_i - \vec{r}_j|} \tag{2.6}$$

where $\hat{V}_{en}(\vec{r}_i)$ is the electron-nucleus interaction term

$$\hat{V}_{en}(\vec{r}_i) = -\sum_{i,I} \frac{Z_I}{|\vec{r}_i - \vec{R}_I|} \tag{2.7}$$

The Electronic Density

Despite these approximations, solving the Hamiltonian in Eq. 2.6 is still a tough problem due to the complexity of wavefunctions with three dimensions. As mentioned previously, the electronic density is introduced instead to simplify the mathematical treatment. The density is obtained by calculating the expectation value of the single particle density operator expressed in Eq. 2.8 with respect to many-body wavefunction as shown in Eq. 2.9.

$$\hat{n}(\vec{r}) = \sum_{i=1}^{N} \delta(\vec{r} - \vec{r}_i) \tag{2.8}$$

$$\begin{aligned} \langle \Psi | \hat{n}(\vec{r}) | \Psi \rangle = & \sum_i \int |\Psi(\vec{r}_1, \cdots, \vec{r}_N)|^2 \delta(\vec{r} - \vec{r}_i) d\vec{r}_1 \cdots d\vec{r}_N \\ & = \int |\Psi(\vec{r}, \vec{r}_2 \cdots, \vec{r}_N)|^2 d\vec{r}_2 d\vec{r}_3 \cdots d\vec{r}_N \\ & + \int |\Psi(\vec{r}_1, \vec{r}, \vec{r}_3 \cdots, \vec{r}_N)|^2 d\vec{r}_1 d\vec{r}_3 \cdots d\vec{r}_N + \cdots \\ & = N \int |\Psi(\vec{r}, \vec{r}_2, \cdots, \vec{r}_N)|^2 d\vec{r}_2 d\vec{r}_3 \cdots d\vec{r}_N \\ & \equiv n(\vec{r}) \end{aligned} \tag{2.9}$$

Here $\vec{r_i}$ defines the position of each indistinguishable electron and due to the assumption of normalization of the wavefunction, an integral of the density over the entire space would yield the total number of electrons.

2.2 The Total Energy

The total energy many-body system must be reformulated in a rather complicated form by employing the density representation. The expressions for all terms of Hamiltonian in Eq. 2.6 are examined one-by-one below in terms of density by taking the expectation values of each operator. First the expectation value of Coulombic electron-nucleus interaction operator by utilizing the many-body wavefunction

$$E_{ne} = \langle \Psi(\vec{r}_1, \cdots, \vec{r}_N) | \hat{V}_{ne} | \Psi(\vec{r}_1, \cdots, \vec{r}_N) \rangle \tag{2.10}$$

Then employing the definition of density at Eq. 2.9 yields;

$$E_{ne} = -\sum_{I}^{N_n} \left[\int \frac{Z_I}{|\vec{r}_1 - \vec{R}_I|} n(\vec{r}_1) + \int \frac{Z_I}{|\vec{r}_2 - \vec{R}_I|} n(\vec{r}_2) + \cdots \right] \tag{2.11}$$

Here the position variables can be replaced with a dummy variable $\vec{r}$ reducing the equation N_e equal electron-interaction terms. Eq. 2.11 can be simplified as

$$\begin{aligned} E_{ne} &= -\sum_{I}^{N_n} \int \frac{Z_I}{|\vec{r} - \vec{R}_I|} n(\vec{r}) d\vec{r} \\ &= \int n(\vec{r}) \hat{v}_{ne}(\vec{r}) d\vec{r} \end{aligned} \tag{2.12}$$

Other terms of Hamiltonian can not be converted in exact way due to fact that the operators in question have either two-body terms or contain a derivative operator as in the case of kinetic energy. Let us start out with the electron-electron interaction term. The expectation value of the relevant operator is

$$\langle\Psi(\vec{r}_1,\cdots,\vec{r}_N)|\hat{V}_{ee}|\Psi(\vec{r}_1,\cdots,\vec{r}_N)\rangle = \frac{1}{2}\sum_{i}^{N_e}\sum_{i\neq j}^{N_e}\int \hat{V}_{ee}|\Psi(\vec{r}_1,\cdots,\vec{r}_N)|^2 d\vec{r}_1\cdots d\vec{r}_N \tag{2.13}$$

where the prefactor $\frac{1}{2}$ is introduced in order to prevent double-counting. We developed Eq. 2.13 by means of explicitly writing out some of terms in the sum

$$\begin{aligned} E_{ee} = \frac{1}{2}[&\int \frac{Z_I}{|\vec{r}_1-\vec{R}_I|}d\vec{r}_1 d\vec{r}_2 \int |\Psi(\vec{r}_1,\cdots,\vec{r}_N)|^2 d\vec{r}_3\cdots\vec{r}_N \\ &+\int \frac{Z_I}{|\vec{r}_2-\vec{R}_I|}d\vec{r}_1 d\vec{r}_3 \int |\Psi(\vec{r}_1,\cdots,\vec{r}_N)|^2 d\vec{r}_2 d\vec{r}_4\cdots\vec{r}_N + \cdots] \end{aligned} \tag{2.14}$$

There are $N_e(N_e-1)$ term in the sum in Eq. 2.14 and by manipulating the integral we obtain

$$E_{ee} = \int \frac{1}{|\vec{r}-\vec{r\prime}|}d\vec{r}d\vec{r\prime}[\frac{N_e(N_e-1)}{2}\int \Psi(\vec{r},\vec{r\prime})d\vec{r}_3 d\vec{r}_4\cdots d\vec{r}_N] \tag{2.15}$$

where the right hand side term corresponds to two particle density as shown at Eq. 2.16 and it consists of both the correlated and uncorrelated portions.

$$\frac{N_e(N_e-1)}{2}\int |\Psi(\vec{r},\vec{r\prime},\cdots,\vec{r}_N)|^2 d\vec{r}_3 d\vec{r}_4\cdots d\vec{r}_N \equiv n^{(2)}(\vec{r},\vec{r\prime}) \tag{2.16}$$

Up to this point, the treatment presented above has been exact. However, the pactical implementation of DFT relies on the expression of each term in the energy in terms of the single-particle density. Fortunately, in large systems, the uncorrelated part of the two-particle density is much larger than the correlated part. In order to facilitate the use of this observation in out equations, we separate these two parts as:

$$n^{(2)}(\vec{r},\vec{r\prime}) = n(\vec{r})n(\vec{r\prime}) + \triangle n^{(2)}(\vec{r},\vec{r\prime}) \tag{2.17}$$

where $\Delta n^{(2)}(\vec{r},\vec{r\prime})$ is the correction term. Following this conversion the electron-electron interaction energy can be expressed as

$$E_{ee} = -\frac{1}{2}\int\int\frac{n(\vec{r})n(\vec{r\prime})}{|\vec{r}-\vec{r\prime}|}d\vec{r}d\vec{r\prime} + \triangle E_{ee} \tag{2.18}$$

where the first term on the right hand side corresponds to Hartree energy E_H and $\triangle E_{ee}$ is the correction term for energy.

The expectation value of kinetic energy operator also needs special consideration, since it contains a derivative term. In order to eliminate this problem electron density is defined as a collection of non-interacting particle orbitals, refered to as the Kohn-Sham orbitals $\phi_n(\vec{r})$. The single-particle orbitals are defined and determined with the same logic of Hartee-Fock formalism with the difference that the density defined by utilizing these non-interacting particles should be in consistent with the ground density of the real system. The density as a sum of norm squares of single particle orbitals is;

$$n(\vec{r}) = \sum_{n}^{N_e}|\phi_n(\vec{r})|^2 \tag{2.19}$$

This is the so-called Kohn-Sham ansatz. The kinetic energy as a function of these orbitals can be expressed as

$$T = -\frac{1}{2}\sum_{n}^{N_e}\int \phi_n^*(\vec{r})\,\nabla^2\,\phi_n(\vec{r})d\vec{r} + \triangle T \tag{2.20}$$

The first term on the right-hand side is slit into two terms: the kinetic energy of the noninteracting system of particles and the difference between this and the true ground state energy, T. Then the total energy in terms of density becomes

$$
\begin{aligned}
E &= -\frac{1}{2}\sum_{n}^{N_e}\int \phi_n^*(\vec{r})\,\nabla^2\,\phi_n(\vec{r})d\vec{r} + \int n(\vec{r})V_{ne}(\vec{r})d\vec{r} \\
&+ \frac{1}{2}\int\int \frac{n(\vec{r})n(\vec{r\prime})}{|\vec{r}-\vec{r\prime}|}d\vec{r}d\vec{r\prime} + \triangle T + \triangle E_{ee} \\
&= T + V_{ext} + V_H + E_{xc}
\end{aligned}
\tag{2.21}
$$

As a result, the exact transformation can be achieved from wavefunction to density except the additional $\triangle T + \triangle E_{ee}$ part of the equation which is defined as the *exchange-correlation* energy E_{xc}.

2.3 Exchange-Correlation Functionals

Exchange-correlation energy represented at Eq. 2.21 as a correction term consists of the exchange energy $\triangle E_{ee}$ which arises from Pauli repulsion between electrons and the correlation term $\triangle T$ arises from the dynamic correlation [30]. Expressed in another way, E_{xc} is the difference between the exact total energy of real system and the Hartree energy of non-interacting Kohn-Sham orbitals. The main complication of DFT while calculating the ground state energy occurs while determining the system E_{xc} accurately. In fact, the accuracy of the particular DFT calculation depends principally upon the sophistication of the exchange-correlation approximation used. There are two fundamental approximations developed with this purpose are the so-called Local Density Approximation (LDA) and Generalized Gradient Approximation (GGA).

The main idea behind LDA is assuming that the actual system density is smooth enough that it is justifiable to treat it as a locally homogeneous electron gas. For the implementation of LDA, the nonhomogeneous, real system is imagined to be divided into infinitesimally small uniform cells with an assumption of having constant density $n(\vec{r})$. Adding up the contributions of energy per particle, $\epsilon_{xc}(n)$ of each cell yields

$$
E_{xc}^{LDA}[n] = \int n(\vec{r})\epsilon_{xc}[n]d\vec{r} \tag{2.22}
$$

which is an expression of E_{xc} directly in terms of density. In this simple approximation , exchange energy is overestimated while correlation term is underestimated. However, the LDA approach still valuable for the description of the bulk properties with uniform charge densities.

The accuracy of the LDA predictions cam be improved significantly by means of including not only the single particle density but also the gradient of density which includes some of the nonhomogeneous character of the true density in a semilocal manner. This approach is referred as the generalized gradient approximation (GGA) and is more eligible for non-uniform systems.

$$E_{xc}^{GGA}[n] = \int n(\vec{r})\epsilon_{xc}[n(\vec{r}), \bigtriangledown n(\vec{r})]d\vec{r} \tag{2.23}$$

Several kinds of functionals have been devepoled based on GGA by manipulating the terms in the square-bracket at Eq. 2.23 in order to describe different kind of systems and the most popular one is PBE(Perdew, Burke and Ernzerhof) [31]. These semilocal functionals are fairly accurate in the calculation of geometry, elastic and band structure of materials with good description of ionic, metallic and covalent bonds. However due to the enormous representation of the long-range behavior of the true electron density, vdW interactions cannot be handled using standard LDA or GGA. This topic shall further be explored in the upcoming sections of this thesis.

2.4 Hohenberg-Kohn Theorem

Two important theorems which established the foundations of DFT were proposed by Hohenberg and Kohn in 1964 [32]. These two theorems can be expressed briefly as follows:

The first theorem states that the external potential of nuclei, V_{ext}, is an unique functional of density. In other words a given density is a non-degenerate ground state density for just one V_{ext} with one-to-one correspondence and another external potential on the system would give rise different density [33].

$$V_{ext} \Leftrightarrow n(\vec{r}) \tag{2.24}$$

The second theorem states that in any quantum state energy is a functional of density and any density other than that of the ground state would lead to a higher energy than ground state energy.

$$E_0[n_0(\vec{r})] < E[n(\vec{r})] \tag{2.25}$$

Here E_0 is the ground state energy and $n_0(\vec{r})$ is the ground state density while E is the total energy written as a functional density $n(\vec{r})$. It follows that one can obtain the ground state density by using the variational principle as minimizing the energy functional with respect to ground state density as follows:

$$\frac{\delta E[n]}{\delta n} = 0 \tag{2.26}$$

2.5 The Kohn-Sham Equations

Kohn-Sham method [34] makes an assumption for electronic density by expressing the real system density using a non-interacting reference system consisting of Kohn-Sham orbitals $\phi_i(\vec{r})$. The expression of density in terms of these auxiliary orbitals is as mentioned at Eq. 2.19. The minimization of the energy by Hohenberg-Kohn variational principle shown at with respect to KS orbitals as shown in Eq. 2.26 yields the orbitals that give rise to ground state energy;

$$\begin{aligned} \frac{\delta E}{\delta \phi_i^*(\vec{r})} &= \frac{\delta T_{ks}}{\delta \phi_i^*(\vec{r})} + \left[\frac{\delta E_{ext}}{\delta n(\vec{r})} + \frac{\delta E_H}{\delta n(\vec{r})} + \frac{\delta E_{xc}}{\delta n(\vec{r})}\right] \frac{\delta n(\vec{r})}{\delta \phi_i^*(\vec{r})} \\ &= \epsilon_i \phi_i(\vec{r}) \end{aligned} \tag{2.27}$$

Here T_{ks} is Kohn-Sham kinetic energy in terms of non-interacting particles adds up to the same value as the real system kinetic energy without the correction term $\triangle T$ included in the exchange-correlation energy E_{xc}. Thus, KS equation can be written in its final form as

$$-\frac{1}{2}\bigtriangledown^2\phi_i(\vec{r}) + [V_{ext}(\vec{r}) + V_H(\vec{r}) + V_{xc}(\vec{r})]\phi_i(\vec{r}) = \epsilon_i\phi_i(\vec{r}) \tag{2.28}$$

where the collection of terms inside the square brackets are denoted as Kohn-Sham potential V_{KS} and the many-body Schrödinger equation becomes:

$$[\hat{T} + \hat{V}_{KS}]\phi_i = \epsilon_i\phi_i \tag{2.29}$$

All the potential terms at KS equation directly depend on the density which means that the potential changes with density which requires to be solved self-consistently as shown at the flowchart in Figure 2.1

2.6 The Plane Wave Basis and The Pseudopotentials

In order to achieve the iterative calculation of Kohn-Sham equations in an accurate and efficient manner one needs to describe the non-interacting electron system in terms of an appropriate basis set of functions. The plane-wave basis (PW) set is usually truncated using the criterion that the largest kinetic energy of a PW in the basis be smaller than a predetermined cutoff energy E_{cut}. The accuracy of the calculation can be tuned by adjusting the E_{cut} in a systematic manner. Despite the simplicity of implementation associated with a PW set, when all electrons in a system are taken into account, a very large PW set is required to resolve the oscillatory behavior near the core region. The pseudopotential approach was introduced in order to tackle this problem.

The electrons of an atom can be classified as "core" and "valence" electrons with respect to the shells they occupy. Core electrons are localized around nuclei with closed

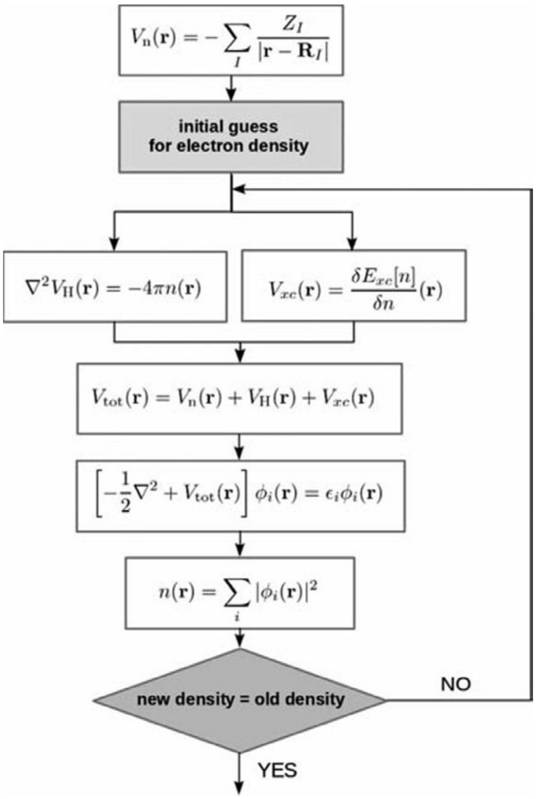

$V_n(\mathbf{r}) = -\sum_I \frac{Z_I}{|\mathbf{r}-\mathbf{R}_I|}$
initial guess for electron density
$\nabla^2 V_H(\mathbf{r}) = -4\pi n(\mathbf{r})$
$V_{xc}(\mathbf{r}) = \frac{\delta E_{xc}[n]}{\delta n}(\mathbf{r})$
$V_{tot}(\mathbf{r}) = V_n(\mathbf{r}) + V_H(\mathbf{r}) + V_{xc}(\mathbf{r})$
$\left[-\frac{1}{2}\nabla^2 + V_{tot}(\mathbf{r})\right]\phi_i(\mathbf{r}) = \epsilon_i\phi_i(\mathbf{r})$
$n(\mathbf{r}) = \sum_i |\phi_i(\mathbf{r})|^2$
new density = old density
NO
YES

Figure 2.1: Kohn-Sham self-consistency cycle

shell orbitals and the relatively distant ones that involve the interactions and chemical bond formation are valence electrons. The wave functions of core and valence electrons are orthogonal to each other and in the core region, $r_c \leq r$, valence wavefunctions display oscillatory behavior as shown in Figure 2.2 with dashed lines. Here it is also seen that the interaction potential V that induces the oscillation in the core region is very large.

Pseudopotential approach is based on the idea of using a pseudo wavefunction Ψ_{pseudo} that acts only on the valence electrons and includes the Coulombic potential of the nucleus and the screening effect of the core electrons. This method is also referred to as the *frozen-core approximation* and relies on the generation a smooth Ψ_{pseudo} for core region to reduce the required PW cut off energy with high accuracy Then the potential V is replaced to a weaker potential V_{pseudo} which has identical valence electron wavefunctions outside the core region $r \geq r_c$. In this thesis ultrasoft pseudopotentials developed by Vanderbilt [35] are used since this method gives an opportunity to use fewer planewaves with high accuracy. The effectiveness of ultrasoft type pseudopo-

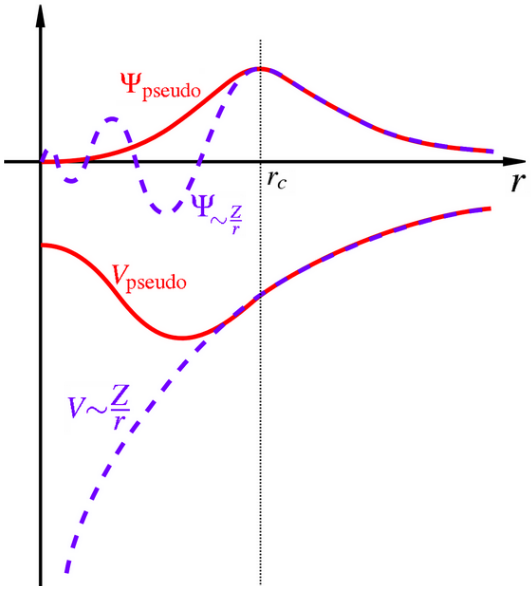

Figure 2.2: Pseudopotential and pseudowave function with respect to real system

tentials for graphene sytsem is examined in detailed at Chapter 3.

2.7 The van der Waals Interaction

Despite the fact that LDA and GGA are sufficient to determine the covalent interactions, vdW forces arising from long-range electron interactions can not expressed accurately by conventional DFT. To fix this inadequacy several approaches have been employed in order to obtain a correct definition of dispersion relation in systems coupled via non-covalent interaction. Dispersive vdW interactions arise from instantaneous dipole fluctuations between neutral fragments of the total system. The simplest approach would be to add an empirical term to the KS energy to represent these interactions:

$$E = E_{KS} + E_{disp} \tag{2.30}$$

where

$$E_{disp} = -\frac{C_6^{IJ}}{R_{IJ}^6} \tag{2.31}$$

The pairwise dispersion energy given in Eq. 2.31 in terms of the distance between weakly interacting species I, J and the dispersion coefficient C_6^{IJ} is the so-called London dispersion. C_6^{AB}, on the other hand, is a function of the ionization potential and polarizability of particles.

DFT-D method developed by Grimme [36] that is one of the earliest corrections built on this pairwise dispersion as

$$E_{disp} = -s_6 \frac{C_6^{IJ}}{R_{IJ}^6} f_6(R_{IJ}) \tag{2.32}$$

This correction regulates the E_{disp} by adding a damping factor as a function of displacement R_{IJ} as seen at Eq. 2.32. $f_6(R_{IJ})$ converges to zero as R_{IJ} approximates to zero or infinity to prevent the diverging repulsive forces when the atoms gets close. The scaling factor s_6 is a parameter that depends on the functional used with DFT-D correction.

DFT-D is an empirical correction and although it gives closer results to experimental values , due to the weakness at calculation of heavy elements, a next generation DFT-D2 method was developed which differs from the previous in its approach to the calculation of the C_6^{IJ} and the scaling parameter. However, DFT-D2 still does not work for metals properly [37]

Since, in reality, the KS and dispersive contributions cannot be separated as shown in Eq. 2.30 an improved correction than pairwise dispersion by introducing a correlation kernel function $K(\vec{r}_1, \vec{r}_2)$ that depends on electron position, density and gradient of density. This method relies on calculating the long range electron interaction in terms of density by both calculating the density variation in distant regions and their correlations. Thus, the exchange correlation energy in the Kohn-Sham equation is redefined with vdW correction where the non-local correlation energy E_c^{nl} is shown at Eq. 2.33 with charge density $n(\vec{r})$.

$$E_c^{nl} = \frac{1}{2}\int\int K(\vec{r}_1, \vec{r}_2) n(\vec{r}_1) n(\vec{r}_2) d\vec{r}_1 d\vec{r}_2 \tag{2.33}$$

The earlier and one of the most popular non-local correction is vdW-DF [38]. The exchange correlation density is arranged as collection of the non-local energy E_c^{nl} and the local or semi-local energy terms calculated using LDA or GGA approximations as

$$E_c^{vdW-DF} = E_c^{LDA/GGA} + E_c^{nl} \tag{2.34}$$

vdW-DF functional is an ab initio approach in contrast with DFT-D type dispersion corrections. However, this method also has some weaknesses such as overestimation of the interaction energy. Functionals such as PBE and revised PBE namely revPBE [39] are commonly preferred for use together with the vdW-DF method. Since the vdW-DF and revPBE combination overestimates the equilibrium interlayer distance at structure optimization due to the repulsive characteristic or revPBE functional, PW86 [40] exchange functional was considered but was also seen to create some drawbacks such as overestimating the binding energy. However, the vdW-DF-C09 [41] correlation with the Cooper correction on the exchange functional and its revised version vdW-DF2-C09 was observed to achieve the agreement with experiment more accurately especially for graphene metal interaction as proposed by Hamada et. al. [42].

In our calculations that will be mentioned in Chapter 3, the vdW interactions between graphene sheets are calculated by employing DFT-D, vdW-DF and VDW-DF2-C09 functionals for purpose of comparison. These preliminary calculations suggest that the Cooper correction provides the closest agreement with experiments and literature.

2.8 Calculation Details

Plane-wave self consistent field (PWscf) approach based the Quantum Espresso (QE) package was utilized for the DFT calculations in this thesis [43]. QE performs self consistent iterative calculations for Kohn-Sham equations with user defined pseudopotential and exchange-correlation selections.

For the graphene/graphene interaction reported in Chapter 3, convergence achieved by implementing the Monkhorst-Pack schemed [44] 12x12x1 k-point grids for a 1x1 unit cell of graphene. A kinetic energy cutoff of 40 Ry for wavefunctions and 400 Ry for charge density are employed.

In Chapter 4, different k-point grids are used with respect to the size of particular unit cells for each Au interface/graphene configuration. All the other calculation parameters remain the same.

2.8.1 Structure Optimization

Geometry optimization is performed in order to determine the minimum energy configuration of the system which satisfies the condition of zero force on all atoms. This structure relaxation relies on the Hellman-Feynman theorem [45],[46] which states that the variation of the energy with respect to atomic positions, directly depends on the variation of Hamiltonian rather than the change in wavefunction. The fundamental steps of the theorem ca be outlined as follows:

$$\begin{aligned}\vec{F}_i = -\frac{\partial E}{\partial \vec{R}_i} &= -\frac{\partial \langle \Psi | \hat{H} | \Psi \rangle}{\partial \vec{R}_i} \\ &= -\langle \frac{\partial \Psi}{\partial \vec{R}_i} | \hat{H} | \Psi \rangle - \langle \Psi | \frac{\partial \hat{H}}{\partial \vec{R}_i} | \Psi \rangle - \langle \Psi | \hat{H} | \frac{\partial \Psi}{\partial \vec{R}_i} \rangle \\ &= -E_i \frac{\partial \langle \Psi | \Psi \rangle}{\partial \vec{R}_i} - \langle \Psi | \frac{\partial \hat{H}}{\partial \vec{R}_i} | \Psi \rangle \\ &= -\langle \Psi | \frac{\partial \hat{H}}{\partial \vec{R}_i} | \Psi \rangle\end{aligned} \tag{2.35}$$

The structure relaxation is implemented in parallel with self consistent calculations. First the net force on each atom is obtained for an initial set of nuclear coordinates by conducting the ground state energy calculations for the given configuration. Then, by changing the positions of nuclei slightly along the direction of the forces, the ground state energy and density are recalculated for the new configuration of atoms. Iterative calculations are performed until a user defined threshold is achieved for the force acting on each atom. The relaxed atomic positions, final values of force and considering ground state energy are stored in output files.

2.8.2 The Calculation of the Friction Force

The friction force under the influence of varying magnitudes of external normal load between graphene layers and Au/graphene interfaces is investigated using the model developed by Zhong and Tomanek [18] for their Pd-graphite system. Brief information about this calculation method can be given as follows:

First the magnitude and variation of normal force as a function of interlayer separation distance of surfaces is obtained

$$F_N = -\frac{\partial E_{ad}(z)}{\partial z} \tag{2.36}$$

where adhesion energy is

$$E_{ad} = E_{tot}(Pd - graphite) - E_{tot}(Pd) - E_{tot}(graphite) \tag{2.37}$$

The position dependency of the interaction energy is calculated as Pd layer slides along a lateral direction over graphite. The potential energy during this motion is calculated as

$$V(x, F_N) = E_{ad}(x, z(x, F_N)) + F_N z(x, F_N) - V_0(F_N) \tag{2.38}$$

where $V_0(F_N)$ is the hollow site configuration energy that would make the potential $V(x, F_N)$ minimum. Subsequently , the position dependent lateral force F_x is introduced in terms of variation of $V(x, F_N)$ along x-direction as;

$$F_x(x, F_N) = \frac{\partial V(x, F_N)}{\partial x} \tag{2.39}$$

The maximum value of F_x corresponds to static friction that leads to stick-slip motion. The maximum potential energy $V_{max}(F_N)$ is reached when the Pd layer is stuck at the edge of the potential energy barrier due to interaction with graphite(stick part). V_{min} is the minimum of the potential energy throughout the motion. Using these values the dissipation energy as a result of friction is

$$E_{disp} = V_{max}(F_N) - V_{min}(F_N) \tag{2.40}$$

where E_{disp} should be lower than or equal to the amount of increase in potential energy $\triangle V$ during stick part of motion, in other words the amplitude of the potential well. The average friction force related to dissipated energy along the x-direction is then defined as

$$\langle F_f \rangle = \frac{\triangle E_{disp}}{\triangle x} \tag{2.41}$$

Thus, the friction coefficient of Pd-graphite system is determined as the ratio of average friction force to external normal load as shown at the Eq. 2.42

$$\mu = \frac{\langle F_f \rangle}{F_N} \tag{2.42}$$

CHAPTER 3

GRAPHENE-GRAPHENE INTERACTION

As a means of gaining insight into the layer number and external load dependency of friction force, benchmark studies were carried out on the graphene-graphene interface. Calculations that will be detailed in this chapter are on monolayer, bilayer and trilayer graphene. As a first step, the lattice constant of graphene was calculated using different vdW protocols. Then geometry optimization tests were conducted in order to obtain the most reliable exchange-correlation functional method to model the van der Waals interaction between graphene layers. Finally the nature of lateral friction force between 2 and 3 graphene layers along the direction of bonds was investigated.

3.1 Graphene Lattice Constant and Separation Distance

Before examining the interactions between graphene-graphene interfaces, the optimum length of the C-C bond was calculated by means of calculating the total energy of a primitive graphene unit cell as a function of the bond length. Further, these calculations were repeated with different exchange-correlation functionals and ultrasoft pseudopotentials in order to investigate the dependence of the bond length on calculation parameters. Tests were performed using the PW91 [47], PBE [31] and PZ [48] flavors of exchange-correlation functionals. The plots of energy vs. C-C bond length are shown in Figure 3.1.

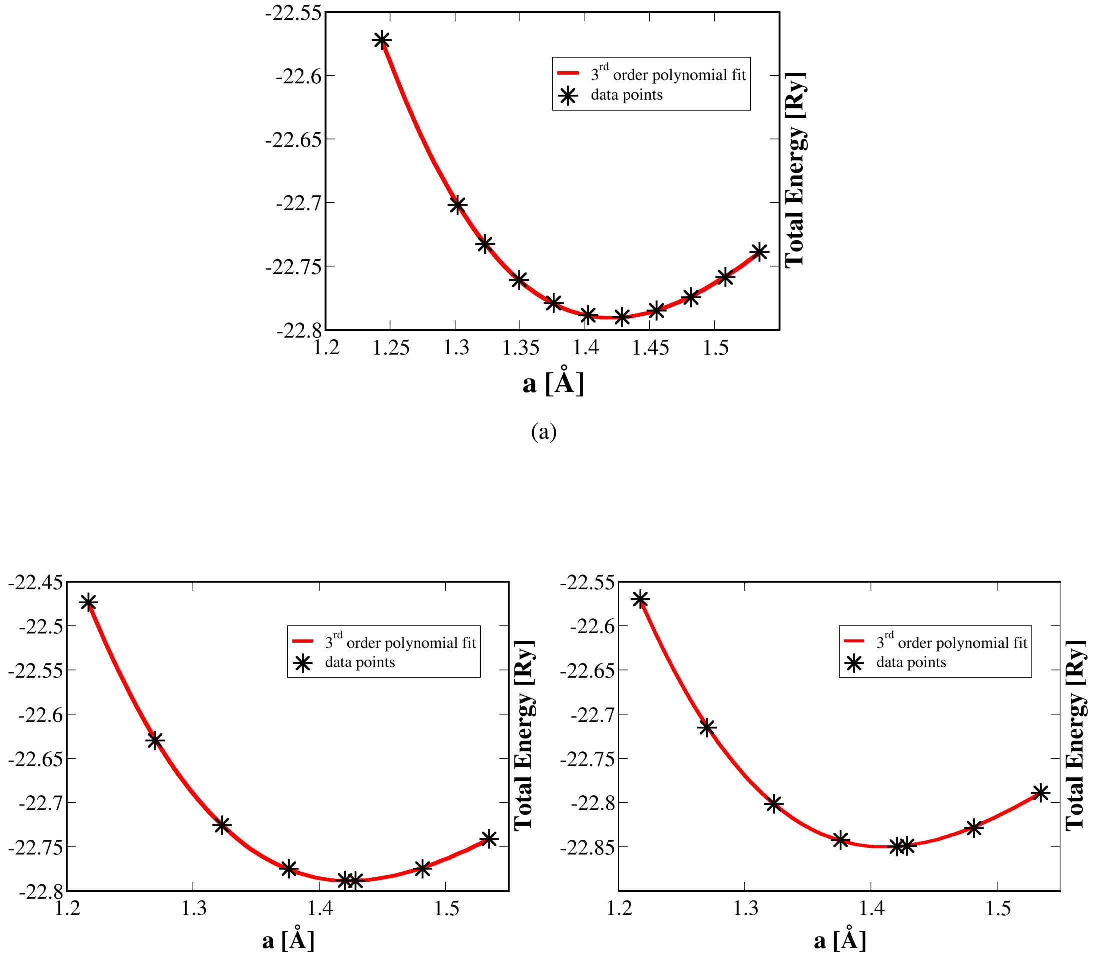

(a)

(b)

(c)

Figure 3.1: Total energy [eV/C-atom] vs lattice constant [$\mathring{A}$] with (a)PBE (b)PW91 (c)PZ pseudopotentials

Among the minimum energy bond length results that are shown in Table 3.1 the PBE approximation provides the most accurate result. Subsequently equilibrium layer separation (d_{eq}) between two graphene sheets was obtained with different exchange-correlation functionals by analyzing the interlayer interaction energy at different distances along the z-direction. Equilibrium separation distance here refers to the relative position of two graphene sheets with minimum energy. During the d_eq calculations the upper layer has been shifted along the z-direction in steps of 0.071$\mathring{A}$ while lower layer is fixed.

Table 3.1: Comparison of experimental and numerically calculated lattice constant of monolayer graphene with different pseudopotentials and calculation errors

Pseudopotential	**Lattice Constant [$\AA$]**	**Error [%]**
PW91	1.4234	0.24
PBE	1.4194	0.04
LDA	1.4120	0.56
exp	1.42	-

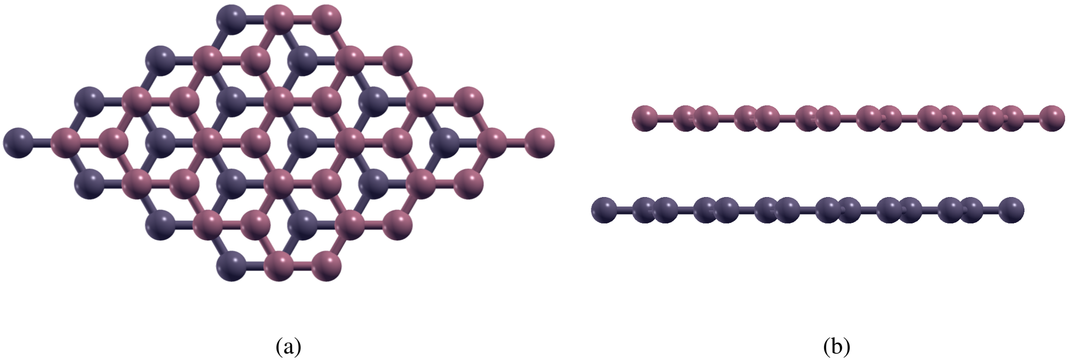
(a) (b)

Figure 3.2: AB-stacked bilayer graphene (a)top view (b) side view

The predominant interaction between layers of multilayer graphene arises due to weak van der Waals forces. In our preliminary calculations, we perform a comperative study of the optimum interlayer distance in bilayer graphene, involving three different van der Waals protocols, namely DFT-D, vdW-DF and vdW-DF2-C09.

Graphene planes were initially constructed in the AB stacking configuration as seen in Figure 3.2 that corresponds to alternating C atoms of the upper layer being in alignment with the hexagonal hollow sites of the lower layer. This configuration is in general energetically most favourable geometry rather than on top and bridge positions. Energy vs distance plots for the three aforementioned vdW protocols with lattice constant optimization are presented in Figure 3.3. Interaction energy presented at of the structure is calculated by

$$\triangle E = (E_{bilayer} - 2E_{monolayer}) \tag{3.1}$$

where $E_{bilayer}$ is the total energy per supercell of the fully optimized graphene bilayer in AB stacking and $E_{monolayer}$ is total energy of one graphene sheet.

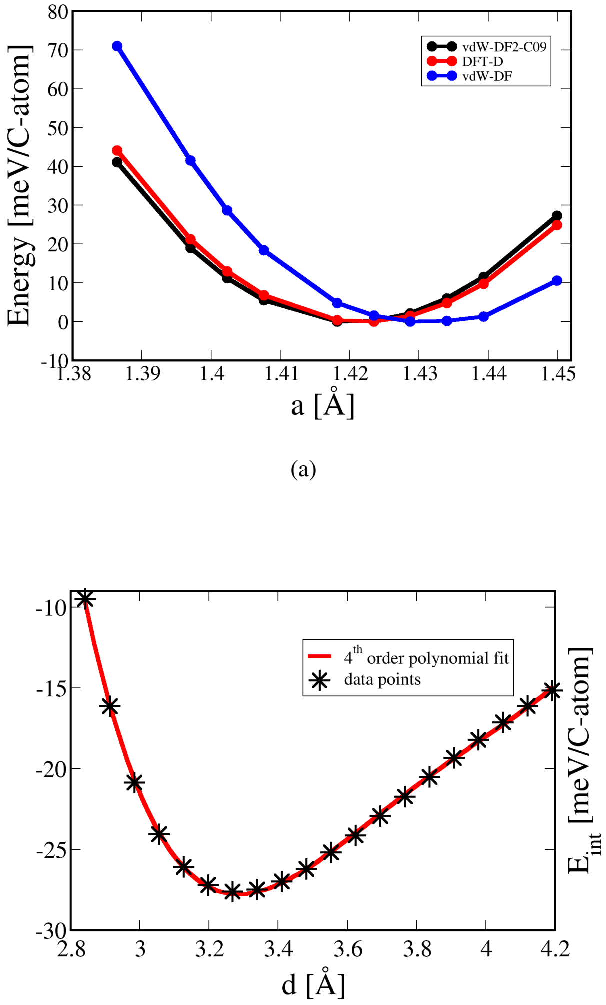

(a)

(b)

Figure 3.3: Graphene (a)C-C bond length evaluated by DFT-D, vdW-DF and vdW-DF2-C09 functionals and (b)layer separation with vdW-DF2-C09 functional

In Figure 3.3(a) comparative total energy values of all three functionals were

Table 3.2: Graphene C-C bond length and equilibrium separation of graphene layers with different vdW protocols. Experimental and previously calculated theoretical values are also included for comparison

Functional	**a [Å]**	**d[Å]**	**d[Å]**
DFT-D	1.422	3.24	3.25[b]
vdW-DF	1.431	3.60	3.62[c]
vdW-DF2-C09	1.421	3.28	3.28
exp.	1.42	3.35[a]	-

[a] [49] [b] [50] [c] [51]

shifted by their minimum for clarity. According to the optimized lattice constant and separation distance values that are presented in Table 3.2, it can be concluded that while DFT-D functional overestimates the C bond length and underestimates the layer separation, vdW-DF overestimates both the lattice constant and the interlayer distance. However, the Cooper correction implemented vdW-DF2-C09 functional provides the most accurate results in comparison to the experimental value and previous *ab-initio* studies presented for both lattice constant and equilibrium separation distance. Despite the fact that for the separation distance vdW-DF2-C09 slightly underestimates the experimental value, our results are consistent with previous theoretical studies. The interaction energy for this configuration is $\triangle E$=-27.612 meV/C-atom for d_{eq}=3.286 with vdW-DF2-C09 functional.

3.2 Potential Energy Surface

As a means of understanding the magnitude of the interaction energy between the graphene layers, the potential energy surface (PES) was mapped within the smallest unit cell. PES calculations were performed by means of successively positioning the upper graphene layer on a fine grid of 0.03 Å points covering the entire unit cell and calculating the energy, while the lower layer was held fixed in space. Calculations were repeated for both DFT-D and vdW-DF2-C09

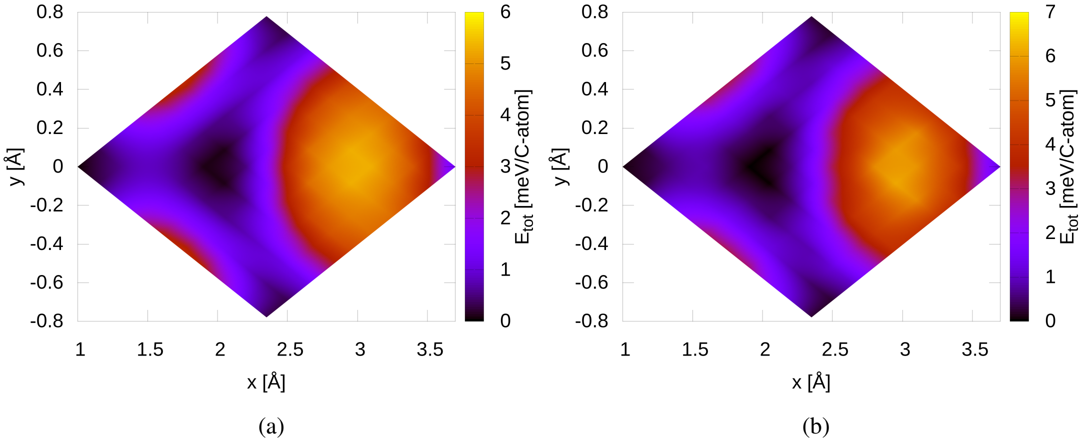

(a)

(b)

Figure 3.4: PES configuration with (a)DFT-D and (b)vdW-DF2-C09 functionals

functionals with equilibrium separation distances provided by each functional. AB stacking geometry was selected as the initial configuration. At each point along the motion of the upper layer with respect to the lower one the vertical force was kept zero by means of geometry optimization in the z-direction during the motion. In the contour plots of the PES profile seen in Figure 3.4 darker regions with the largest interaction represents AB stacking while the lighter one corresponds to on top site geometry.

The total energy values of the bilayer graphene seen at Figure 3.4 were arranged by taking difference between the exact value and the minimum energy provided by each functional in order to present a clear comparison for our results. DFT-D functional yields smaller potential energy corrugation between different stacking configurations of layers while it is more distinct for vdW-DF2-C09. Due to the large degree of symmetry that crystal interfaces possess, our Au-graphene lateral friction force will be gathered only along certain high-symmetry directions. As these directions typically correspond to high commensurability, they should set upper limits to friction forces. As a preliminary example, we next present friction force results along the zigzag direction of the graphene-graphene interface. This direction shall, by convention, be referred to as the "x-direction". The visualisation for sliding movement of upper layer is as can be seen at Figure 3.5.

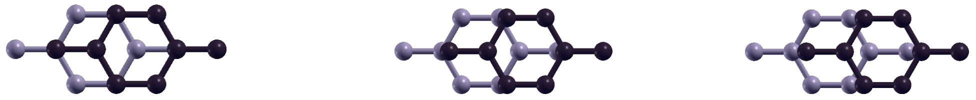

(a) x=0 Å (b) x=1.6756 Å (c) x=1.9312 Å

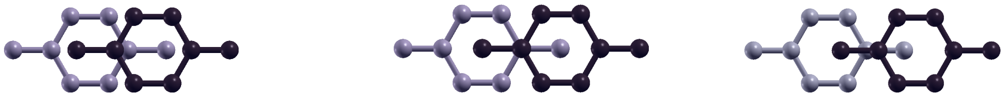

(d) x=2.3572 Å (e) x=2.8684 Å (f) x=3.2944 Å

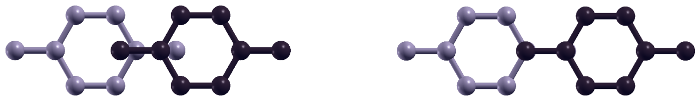

(g) x=3.7204 Å (h) x=4.2316 Å

Figure 3.5: Lateral displacement along the x-direction of the upper graphene layer separated by equilibrium interlayer distance while the bottom layer kept fixed

During the relative motion while keeping the bottom layer fixed, two different approaches were applied to the sliding motion of the upper plane (a) relaxing just along z-direction, (b) allowing geometry optimization in all three directions for each lateral zigzag step. From this point forward, only calculations performed within the vdW-DF2-C09 functional will be reported. For both methods, the maximum interaction is observed for the AB stacking configuration, the smallest interaction for the AA stacking while a smaller local minimum occurs for an intermediate geometry as can be seen at Figure 3.6(a).

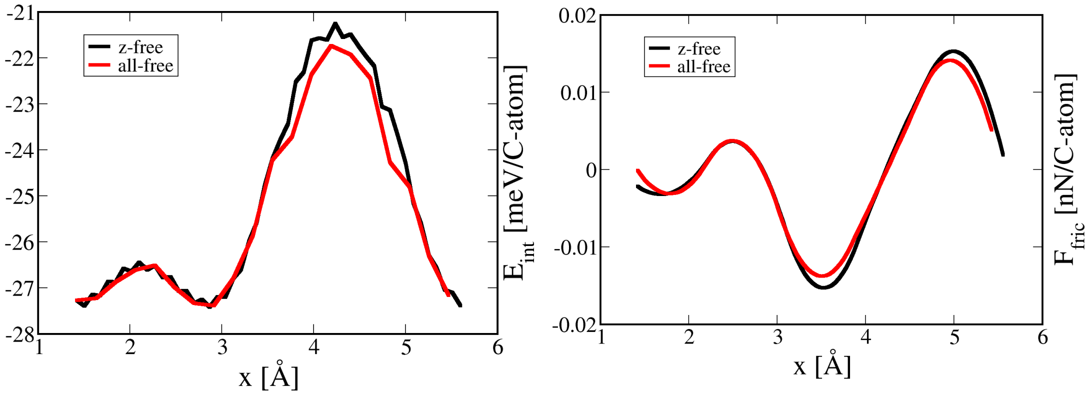

(a)

(b)

Figure 3.6: Lateral energy and friction force for bilayer graphene at different degrees of freedom

As indicated from the comparative results presented at Figure 3.6 the geometrical degree of freedom does not cause a considerable difference in terms of lateral energy and friction forces. Hence, calculations with z-direction optimization only will be preferred hereafter to avoid computational cost.

3.3 Dependence of the Friction Force on the Number of Layers in Graphene Interfaces

Systems with varying numbers of layers were tested in order to investigate the variation of the interaction energy and friction force between graphene sheets. Calculations were done with the vdW-DF2-C09 functional and kinetic energy cut off was set to 40 Ry and a 12x12x1 k-point grids. First of all two layered system was analyzed with initial AB stacking configuration and total zero load on both layers by letting the upper layer free along z-direction as deduced from our previous work for order of geometrical freedom test. Following that, a third graphene sheet was added on top of this bilayer system with ABA stacking configuration keeping the equilibrium interlayer separation distance between the bottom two layers constant. The same procedure was applied for relative motion of uppermost while bottom two layers kept fixed.

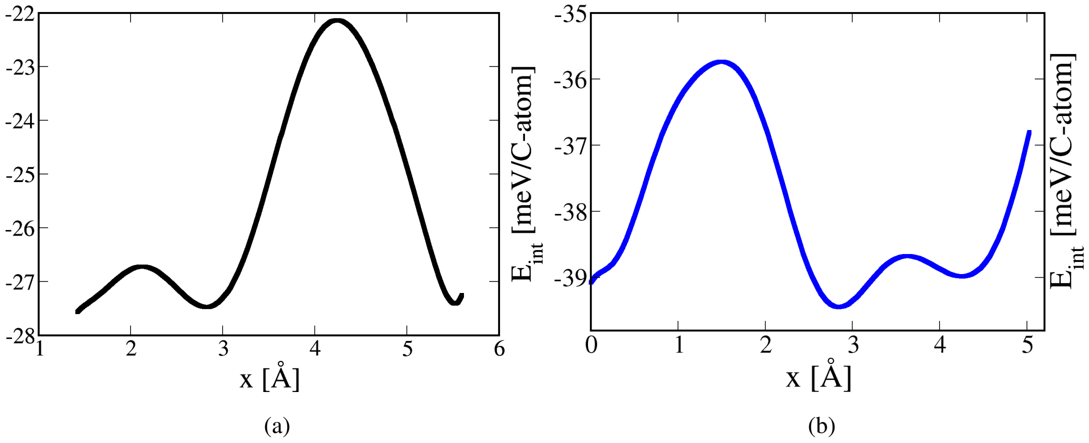

Figure 3.7: Lateral energy variation with respect to layer number for (a) bilayer graphene and (b) trilayer graphene

According to our results the interaction energy per C atoms in a unit cell increases with increasing layer number. As can be seen in Figure 3.7 interaction energy varies from -22 to -28 meV/C atom for bilayer structure whereas the range is -35 to -39 meV/C-atom for the trilayer structure. This observation of increasing interaction energy proportional to number of layer is consistent with the previous studies [52].

Similarly, friction force with respect to relative lateral motion of upper monolayer over mono and bilayer graphene stackings were also investigated. Lateral force results are obtained by evaluating the numerical derivative of energy with respect to lateral displacement are shown in Figure 3.8. Average friction force was calculated by $F_{avg} = \frac{|\sum_i \vec{F_i}|}{N}$ where $\sum_i \vec{F_i}$ is the sum of negative friction values which correspond to the "stick" portion of the stick-slip motion and N is the number of data points along x-direction.

For bilayer graphene average friction was calculated as 0.0105 nN/C-atom as it is 0.0032 nN/C-atom for trilayer system. These comparison reveals that increasing number of layer without any external load makes the friction force lower in agreement with literature.

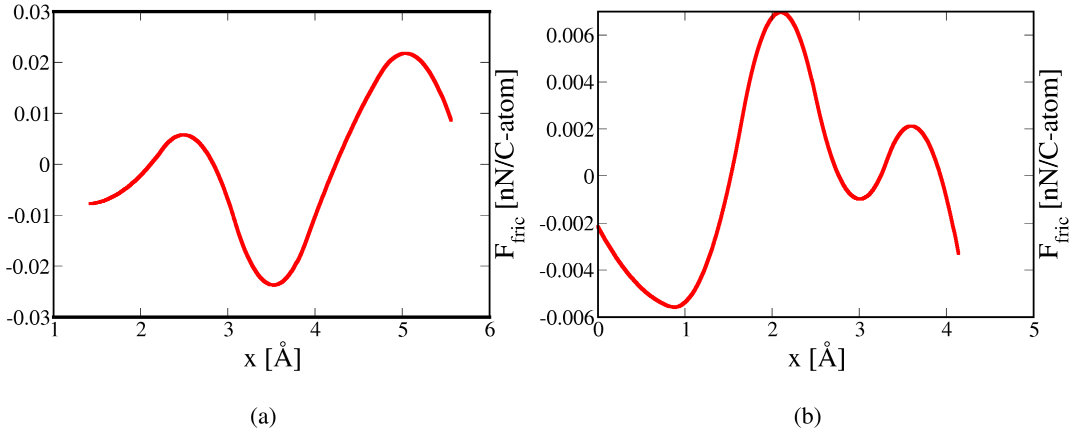

(a)

(b)

Figure 3.8: Friction force variation with respect to number of layer for (a) bilayer graphene and (b) trilayer graphene

3.4 Load Dependency of Friction Force Between Graphene Surfaces

Next, friction behaviour of considered graphene systems under constant load were analyzed. To achieve this, at every relative lateral displacement site, the upper monolayer was shifted in steps of 0.05 along the vertical direction between z_i =3.05 Å and z_f =3.62 Å. Two kinds of calculation methods were used to determine the applied constant load on the system. The first one involves the calculation of the load for each lateral site by taking the derivative of the interaction energy as a function of interlayer separation distance by using Eq. 2.36 as proposed by Zhong et al.[7]

The second method simply utilizes the total force on the upper layer per one unit cell area acquired from the scf calculations performed at distinct interlayer separations. During the relative sliding motion of the graphene layer through one unit cell, variation of the external load with respect to interlayer separation can be seen in Figure 3.9 for some of the lateral sites.

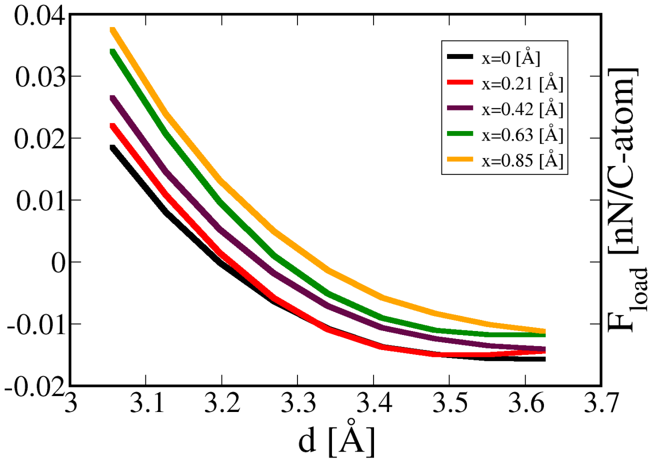

Figure 3.9: Load vs separation distance for bilayer graphene

Table 3.3: Average friction force along x-direction with applied vertical contact force for bilayer graphene

F_{load} **[nN/C-atom]**	F_{avg} **[nN/C-atom]**
0	0.0105
0.01	0.0110
0.02	0.0113
0.03	0.0117
0.04	0.0120
0.05	0.0123

Response of the friction force to the applied load on the bilayer graphene system was examined by comparing the magnitudes of interaction energy and average friction under distinct values load as shown in Figure 3.10(a) and 3.10(b). The variation of average friction force with external load is presented in Table 3.3 and it is concluded that there is a linear proportionality between applied contact force and average lateral friction force which is consistent with the non-adhesive surface model proposed in a previous study [53]. Finally, the friction coefficient of the bilayer graphene system that was obtained with the relation of $\mu = \frac{|F_{fric}|}{F_{load}}$ can be seen in Figure 3.10(b) and using this results one can conclude that friction coefficient between two graphene layers decreases as the applied load increases. Our results shows the inverse proportionality of friction coefficient with applied load in agreement with previous experimental studies [54].

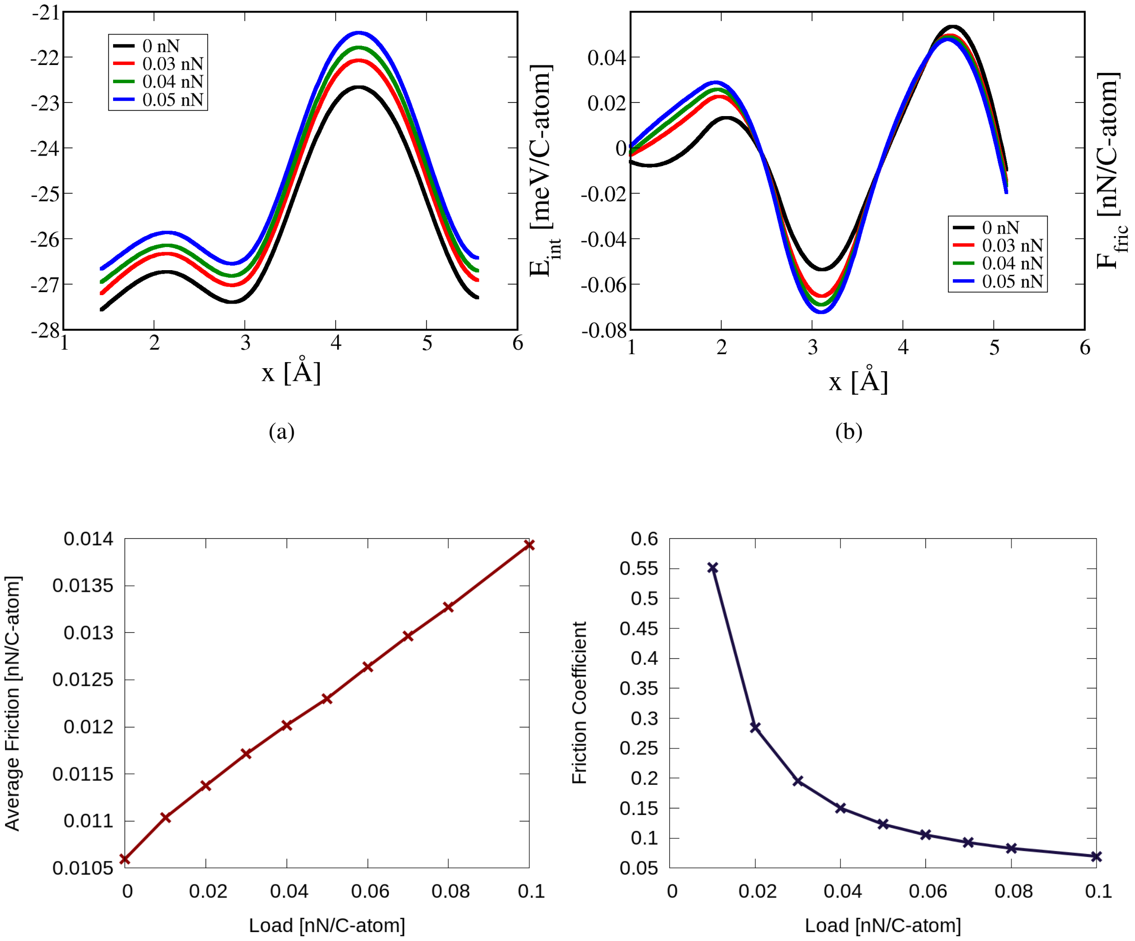

(a) (b)

(c) (d)

Figure 3.10: Load dependency of (a)lateral energy and (b)friction force trend (c)average friction (d)friction coefficient for bilayer graphene

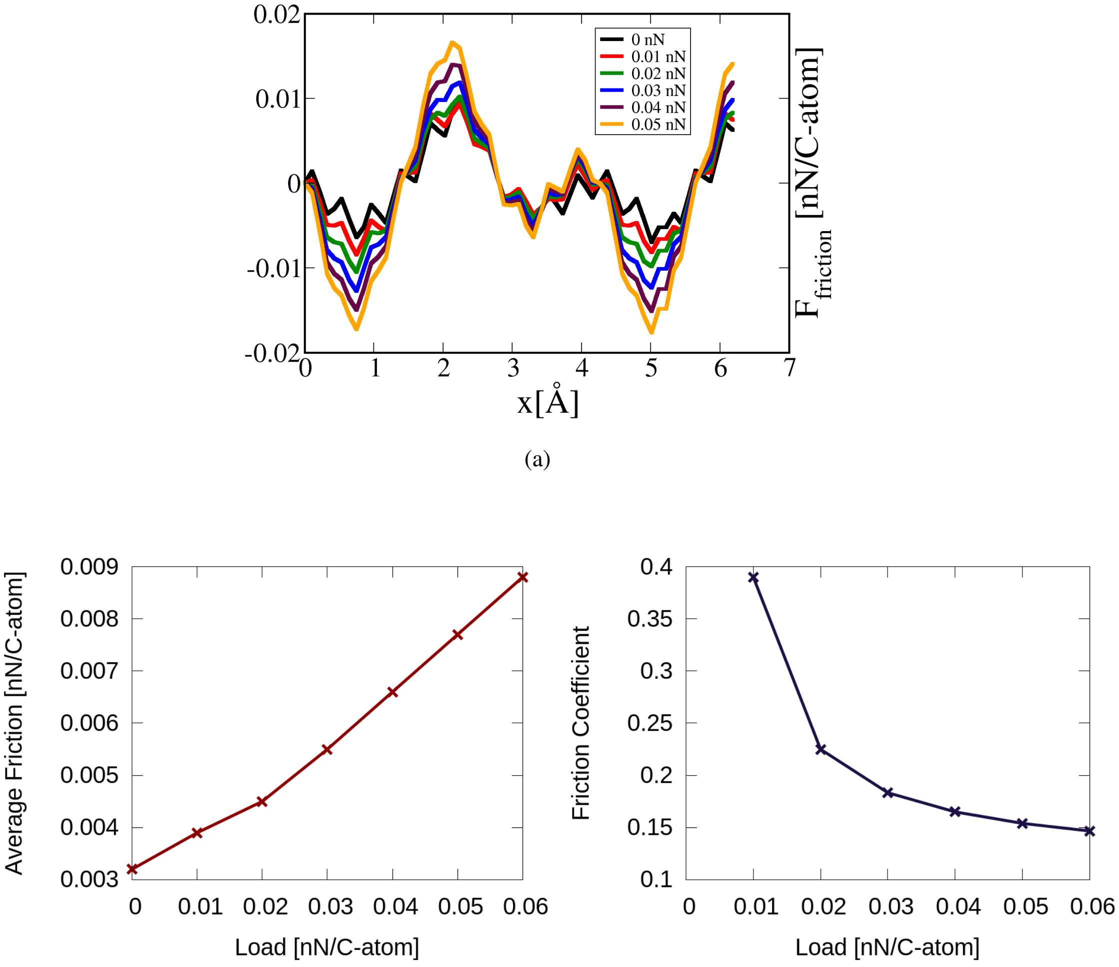

(a)

(b)

(c)

Figure 3.11: (a)Friction force trend and load dependency of (a)average friction and (b)friction coefficient along lateral displacement for trilayer graphene

In addition to bilayer graphene structure, behaviour under external load for the trilayer system was also investigated. The comperative results for applied normal forces are shown at Figure 3.11. The linear proportionality between friction and normal load was observed also for the trilayer graphene, with much lower values than bilayer structure. The obtained average friction values is presented at Table 3.4

Table 3.4: Average friction force of trilayer graphene system along x-direction with applied vertical contact force

F_{load} **[nN/C-atom]**	F_{avg} **[nN/C-atom]**
0	0.0032
0.01	0.0039
0.02	0.0045
0.03	0.0055
0.04	0.0066
0.05	0.0077

CHAPTER 4

AU INTERFACE-GRAPHENE INTERACTION

In this section interaction and friction behaviour at interfaces between graphene and three high symmetry surfaces of Au will be explored. In the friction experiments that inspired this thesis, the FFM tip is covered with Au, as the exact surface that would interact with the graphene sheet cannot easily be known (100), (110) and (111) planes of face centred cubic Au crystal were selected for this study. In order to construct periodic interfaces of graphene and Au, commensurate unit cells must be identified that do not cause excessive strain in either material.

After proper cell configurations were obtained, the lateral sliding calculations of the graphene layer on Au surfaces along the x-direction were conducted under different magnitudes of load. The kinetic energy cutoff was set to 40 Ry for wave functions and 400 Ry for the charge density. vdW interactions were described using the "vdW-DF2-C09" exchange functional and a PBE generated ultrasoft peseudopotential. Brillouin Zone sampling was conducted using different sizes of the Monkhorst-Pack grids according to the dimensions of the commensurate unit cells constructed for each Au interfaces.

4.1 Au Bulk Structure

Before constructing the surfaces, lattice parameters of face centered cubic(fcc) crystal structure of Au were obtained by optimizing the lattice constant. Since there is covalent bond between Au atoms, adding the vdW interaction would not effect the lattice constant but for consistency with following calculations vdW-DF2-C09 type

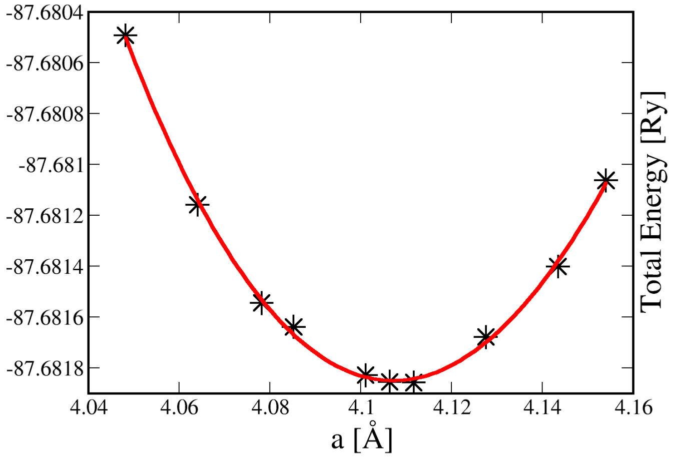

Figure 4.1: Total energy [Ry] vs lattice constant [$\mathring{A}$] of bulk Au

functional was included in the lattice constant calculations. The calculated lattice constant of the Au bulk structure is 4.10803 $\mathring{A}$ with an error of 0.7% with respect to its experimental value of 4.0782 $\mathring{A}$ and the result is as shown at Figure 4.1

4.2 Low-index Surfaces of Au

Crystal surfaces with different orientations are described by utilizing the Miller indices. The Miller indices of a lattice plane are constructed by first determining the non-collinear intersection points along three axis and then taking their reciprocals. In our situations atoms which intercepts the coordinates as (1,∞,∞), (1,1,∞) and (∞,∞,1) gives the (100), (110) and (001) Miller indices respectively by taking the inverse of each intercept. The important point that makes Miller index notation very useful is that, a definition of any plane also represents the other planes parallel to each other through whole crystal lattice [55].

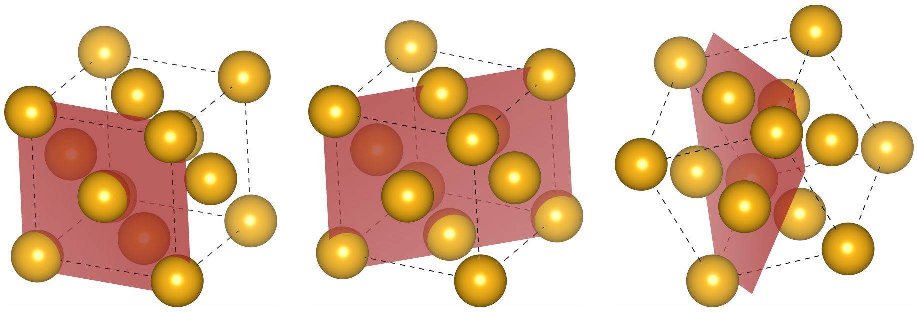
(a) (b) (c)

Figure 4.2: Low index (a)100, (b)110, (c)111 surfaces of fcc Au crystal

The Au(100) surface with four-fold symmetry consists of two layers configured in AB stacking. Basic unit cell of each layer contains one basis atom with four nearest neighbour atoms. In order to construct Au(100) surface, two lattice vectors were determined to generate a single layer. Then the second layer was constructed by shifting the atomic positions of the first layer along x and y directions by $-\frac{1}{2}$ and $-\frac{1}{2}$ in terms of fractional coordinates respectively where the separation between A and B layers determined as $\frac{1}{2}$. Au(100) surface has a square unit cell where the magnitude of lattice vectors is $\frac{a}{\sqrt{2}}$ where a is the lattice constant of the structure. Hence lattice vectors required to construct the (100) surface are

$$\begin{aligned} \vec{u}_1^{100} &= [\frac{a}{\sqrt{2}}, 0, 0] \\ \vec{u}_2^{100} &= [0, \frac{a}{\sqrt{2}}, 0] \end{aligned} \tag{4.1}$$

where the top and side views of Au(100) surface is as shown in Figure 4.3

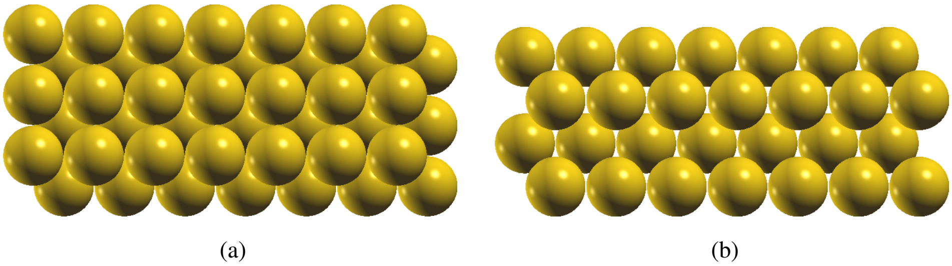
(a) (b)

Figure 4.3: Au(100) surface at (a)on top and (b)side view with ABAB stacking

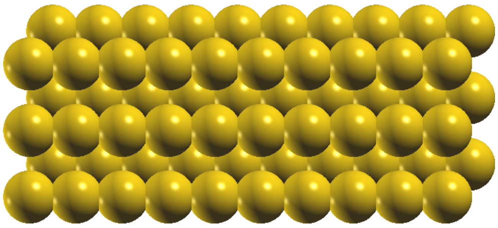

Figure 4.4: Au(110) surface on top view with ABAB stacking

The Au(110) plane with two fold symmetry also represents layers with AB stacking form similar to Au(100) surface. The Au(110) surface has a rectangular unit cell with lattice vectors of length a and $a\frac{\sqrt{2}}{2}$ where a is the lattice constant of Au bulk. Lattice vectors of the surface are

$$\begin{aligned} \vec{u}_1^{110} &= [0, a, 0] \\ \vec{u}_2^{110} &= [\frac{a\sqrt{2}}{2}, 0, 0] \end{aligned} \tag{4.2}$$

Following the construction of one layer using basis atom and lattice vectors acting on it, the second layer can be defined by displacing it along x,y and z directions by $\frac{\sqrt{2}}{4}$, $\frac{1}{2}$ and $\frac{1}{2}$ respectively in terms of fractional coordinates. The top and side views of Au(110) surface are as shown in Figure 4.4

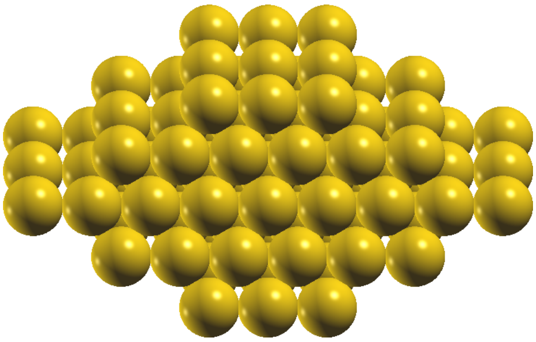

Figure 4.5: Au(111) surface on top view of ABC stacking

The Au(111) surface can be determined as the close-packed construction of the fcc bulk structure and is one of the smoothest low-index surface. The lattice vectors that form reproducing a rhombohedral unit cell are

$$\begin{aligned} \vec{u}_1^{111} &= [\frac{a\sqrt{2}}{2}, 0, 0] \\ \vec{u}_2^{111} &= [\frac{a}{\sqrt{8}}, \frac{a\sqrt{3}}{\sqrt{8}}, 0] \end{aligned} \tag{4.3}$$

Similarly to the other surfaces, following the construction of the first layer, the second layer was constructed by shifting the first one along y-z plane with the vector by $[0, \frac{-a}{\sqrt{6}}, \frac{a}{\sqrt{3}}]$. Then uppermost third layer was constructed by displacing the first layer by $[0, \frac{a}{\sqrt{6}}, \frac{2a}{\sqrt{3}}]$. The basis atoms of the unit cell are $(0,0,0)$,$(\frac{\sqrt{2}}{2},0,0)$ and $(\sqrt{2},0,0)$ in terms of fractional coordinates. Top view of the three layered Au(111) surface is presented at Figure 4.5.

4.3 Graphene on Au interface

4.3.1 Geometry Optimization

In order to provide commensurability for each interface two kinds of method were tested. In the first method, we simple try to minimize the percent strain on either material. In the second method, we consider the average lattice constant for graphene and Au bulk structure and apply the common lattice vectors to construct the proper unit cell for each one. As mentioned in previous calculations the lattice constant for Au bulk was obtained as $a_{Au} = 4.1080\ \AA$ while $a_{graphene} = 1.4210\ \AA$ with the vdW-DF2-C09 density functional. The graphene unit cell was arranged in rectangular shape for (100) and (110) surfaces where original two-dimensional rhombus geometry is kept for the (111) geometry.

The intermediate lattice constant method was implemented for the Au(100) surface where $a_{avg} = \frac{a_{gr}+a_{Au}}{2}$ was determined to be 2.76452 $\AA$. For the Au(100) surface a_{Au} was compressed with a 0.943% error where $a_{Au}^{new} = 4.14677\ \AA$ and a square unit cell was formed with a new lattice constant defined by $3a_{avg} = 2a_{Au}^{new}$. For graphene layer new lattice constant was selected as $a_{gr}^{new} = 1.38\ \AA$ by compressing the structure with a 2.72% error. Rectangular shaped unit cell of graphene was constructed with four basis atoms and also stretching one of the the lattice vector along x direction with 6% error additional to intermediate lattice constant method.

Table 4.1: Percentage error for adjustment of Au(100) and graphene surface unit cells

	a_x	a_y
Au(100)	+0.943%	+0.943%
Graphene	-3.170%	-2.726%

The best matched unit cells for this interface are as shown at Figure 4.6. Overall error during matching the unit cell of interfaces are as presented at Table 4.1.

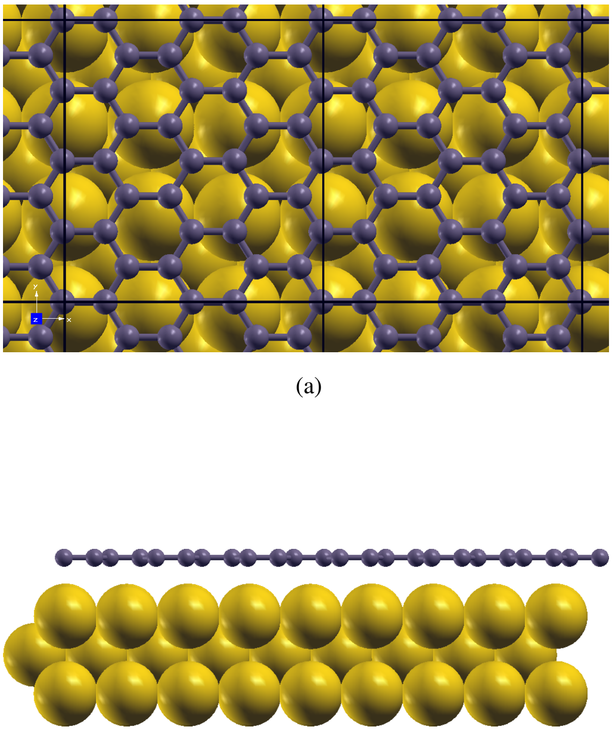
(a)

(b)

Figure 4.6: Graphene and ABA stacked Au(100) unit cell configuration (a)on top and (b)side view

The construction results in a simulation cell that consists of 32 Au atoms with lattice vectors

$$\vec{v}_1^{100} = [8.79, 0, 0] \tag{4.4}$$
$$\vec{v}_2^{100} = [0, 9.57, 0]$$

For the Au(110)-graphene system also a rectangular common unit cell was arranged with previously computed lattice constants for the graphene layer and Au bulk. After Au(110) surface was constructed by the lattice vectors

$$\vec{u}_1^{Au} = [0, 1, 0] \tag{4.5}$$
$$\vec{u}_2^{Au} = [\sqrt{2}/2, 0, 0]$$

with one basis atom, in order to match the unit cell with graphene Au(110) was compressed along the x direction by 0.62% and stretched along y direction by 1.97%. For graphene a rectangular unit cell also constructed by the lattice vectors

$$\vec{u}_1^{gr} = [3, 0, 0] \tag{4.6}$$
$$\vec{u}_2^{gr} = [0, \sqrt{3}, 0]$$

with four basis atoms. In addition the graphene layer was also rotated by 90° clockwise on the Au(110) and the graphene unit cell was also modified by compressing along both x and y directions by 0.86% and 1.03% respectively. The list of per cent deviation of the lattice constants from their original configuration is presented in Table 4.2. The matching graphene and Au(110) conventional cell are as shown in Figure 4.7.

Table 4.2: Percentage error for adjustment of Au(110) and graphene surface unit cells

	a_x	a_y
Au(110)	+0.60%	+1.97%
Graphene	-0.86%	-1.03%

The lattice vectors of constructed simulation cell that consists of 24 Au atoms are

$$\vec{v}_1^{110} = [14.61, 0, 0] \tag{4.7}$$
$$\vec{v}_2^{110} = [0, -4.19, 0]$$

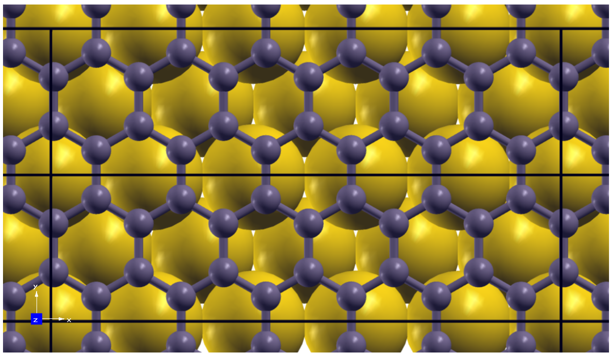

(a)

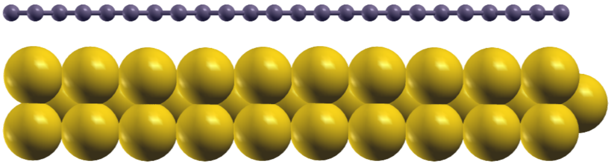

(b)

Figure 4.7: Graphene and ABA stacked Au(110) unit cell configuration (a)on top and (b)side view

For the Au(111) geometry both graphene and Au interface constructed has the same rhombus cell configuration of graphene. Graphene unit cell was constructed by using

Table 4.3: Percentage error for adjustment of Au(111) and graphene surface unit cells

	a_x	a_y
Au(111)	-2.37%	0%
Graphene	-0.18%	-0.18%

the lattice constant $a_{gr} = 1.4184$ $\AA$ which differs from its computed value by 0.18%. After graphene sheet was placed on top of ABCAB stacked five layered Au(111) interface, Au unit cell was compressed along the x direction by 2.37%. Completely matching graphene and Au(111) conventional cell is as shown at Figure 4.8 and the magnitude of deviation in construction from original structures are as seen at Table 4.3.

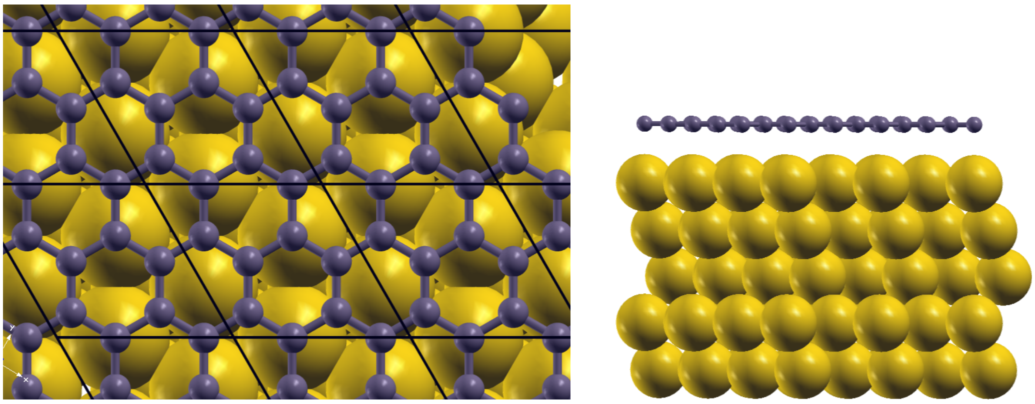

(a) (b)

Figure 4.8: Graphene and ABCAB stacked Au(111) unit cell configuration (a)on top and (b)side view

The constructed simulation cells consist of 15 Au atoms with the lattice vectors as

$$\vec{v}_1^{111} = [4.25, 2.45, 0] \tag{4.8}$$

$$\vec{v}_2^{111} = [4.25, -2.45, 0]$$

4.3.2 Equilibrium Separation Distance

Before determining the minimum energy interlayer separation, internal geometry optimization was performed for each of the three systems with a tight convergence threshold. In the cases for three layered Au(100) and Au(110) configurations all Au layers were let free while at five layered Au(111) interface the bottom two layers were kept fixed and uppermost three layers were relaxed with the graphene sheet. In this part of the chapter equilibrium separation distance between graphene monolayer and each Au surface will be examined separately. The corresponding minimum interaction energy was calculated using

$$E_{int} = E_{tot} - (E_{Au_{surf}} + E_{gr}) \tag{4.9}$$

where E_{tot} is total energy, E_{gr} is energy of one graphene layer and $E_{Au_{surf}}$ is the energy of the multilayered Au interface. Graphene layer was initially positioned at the most favorable hollow site configuration on the along x-y plane for all three systems. The graphene layer was shifted along z-direction incrementally in steps of 0.05 $\AA$ while coordinates of Au interfaces remained fixed.

In the Au(100) case the Brillouin Zone was sampled with 12x12x1 k-points. The equilibrium interlayer separation corresponding to minimum interaction energy was calculated to be $d_{eq} = 3.122$ $\AA$ as a result of 3^{rd} degree polynomial fit with $E_{min} = -59.980$ meV/C-atom. Brillouin zone sampling of Au(110)-graphene unit cell was performed with 8x24x1 k-grids. The separation between graphene and ABA stacked three layered Au(110) surface was found to be $d_{eq} = 3.0976$ $\AA$ as a result of 4^{th} degree polynomial fit with minimum energy $E_{min} = -52.515$ meV/C-atom. Equilibrium interlayer distance between rhombus type unit cell configuration of Au(111) surface and graphene monolayer was obtained as $d_{eq} = 3.3837$ $\AA$ with $E_{min} = -59.781$ meV/C-atom. This calculation, on the other hand, was performed with a 24x24x1 k-point grid. Results of our analysis are as shown in Figure 4.9 and Table 4.4

Table 4.4: Equilibrium separation distance and interaction energy between graphene and Au(111), Au(110), Au(100) interfaces

Interface	**d[$\AA$]**	E_{int}**[meV/C-atom]**
Au(111)	3.384	-59.781
Au(110)	3.098	-52.515
Au(100)	3.122	-59.980

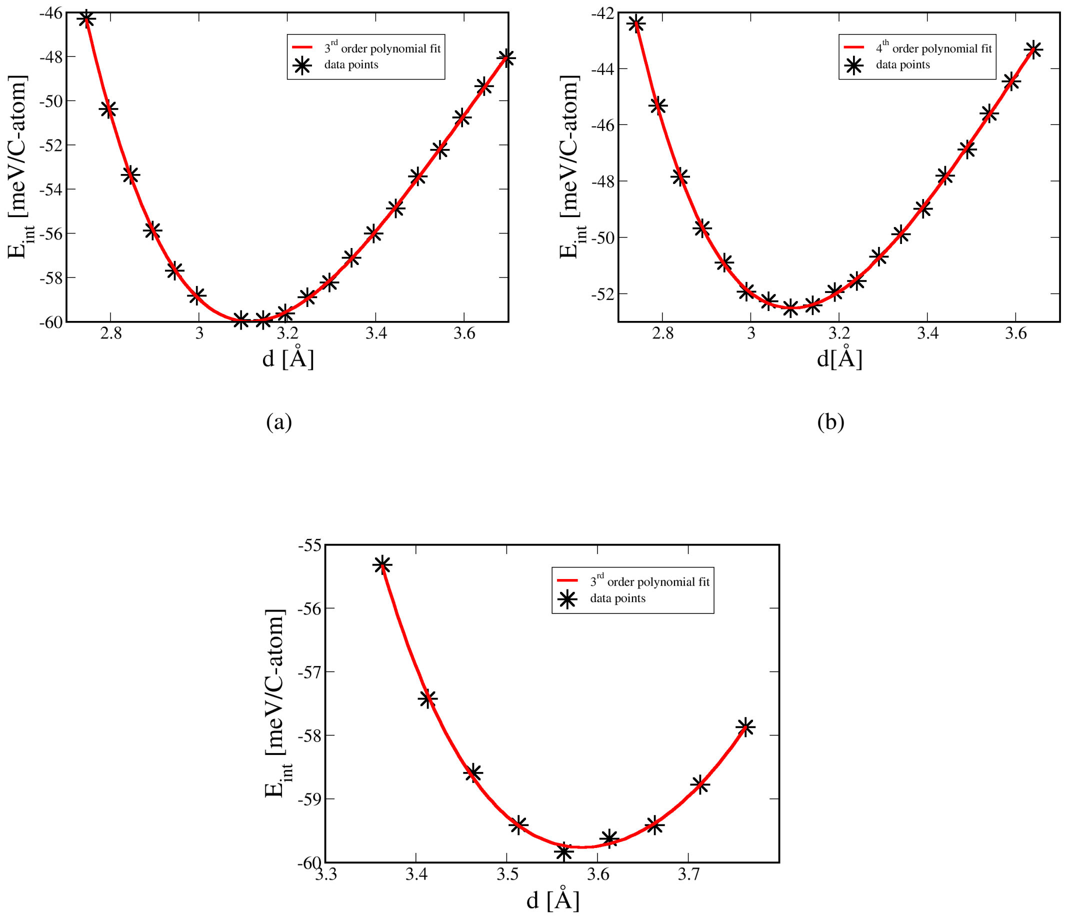

(a)

(b)

(c)

Figure 4.9: Equilibrium separation distance for (a)Au(100), (b)Au(110) and (c)Au(111) surfaces and graphene monolayer

4.3.3 Load Dependence of Energy and Friction Force

In order to observe the effect of external applied load along z-direction on the interaction energy and tribological behaviour of the graphene-Au system a detailed analysis of interaction between surfaces during lateral sliding motion of graphene over the Au interface under several magnitudes of load will be presented in this part. The friction force and coefficient calculations under load used in this chapter is the same one implemented for the benchmark calculations mentioned in Chapter 3. The illustration of lateral sliding motion of graphene over Au interfaces can be seen in Figure 4.10.

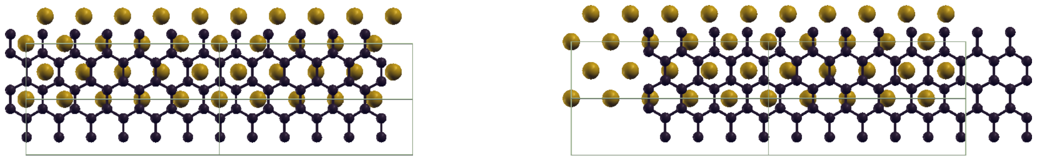

x=-1.14 Å

x=5.75 Å

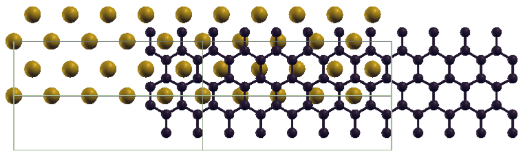

x=10.59 Å

Figure 4.10: Lateral displacement sites of graphene over Au(110) interface

4.3.3.1 Au(100) Interface

As the vertical load is increased on graphene both the interaction energy between materials and friction force shows an increasing trend according to our results that can be seen at Figure 4.11. Applied contact force larger than 0.005 nN induces positive interaction energy which means surfaces get so close that their electrons overlap and repulsive force becomes considerable between materials.

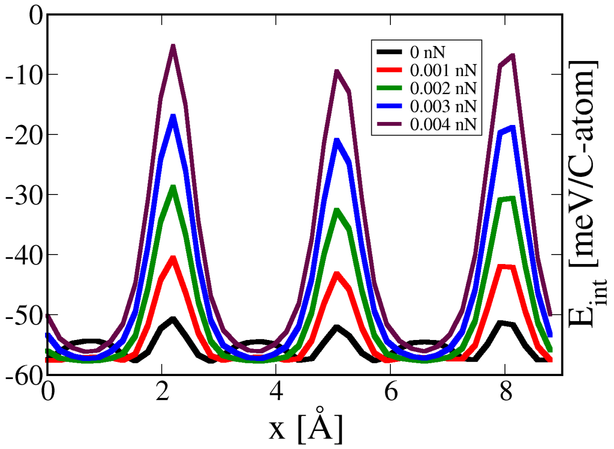

(a)

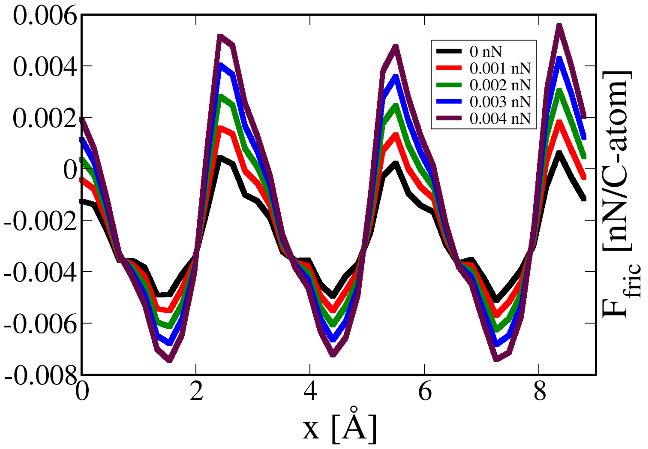

(b)

Figure 4.11: (a) Interaction energy (b)lateral friction force of vertically loaded Au(100)-graphene structure in several orders

Table 4.5: Average friction force between Au(100) and graphene monolayer along x-direction with applied vertical contact force

F_{load} **[nN/C-atom]**	F_{avg} **[nN/C-atom]**
0	0.0026
0.001	0.0027
0.002	0.0030
0.003	0.0034
0.004	0.0038

As the magnitude of the normal load increases, it is observed that a remarkable increase occurs at maximum points of the potential well while minimum interaction points do not vary significantly. According to Figure 4.11(a) it can also be concluded that applied load suppresses the potential wells in particular regions between two maximum values of energy, compared to zero load condition. Results from five different loads for both friction coefficient(μ) and average friction force(F_{avg}) were comparatively examined as can be seen in Figure 4.12. F_{avg} appears to have a linear dependence on external load except the values between 0-0.001 nN where the actual values can be seen at Table 4.5. However, upon closer inspection, the friction coefficient displays a decreasing trend. The reason behind that behaviour was also investigated by analysing the charge density differences between materials during stick-slip motion at corresponding loads.

In order to understand the relation between friction force and the electronic charge distribution along the relative sliding motion, the average charge density of the system is investigated under 0 nN/C-atom and 0.001 nN/C-atom loaded conditions. The average charge variation regarding to stick and slip portions of the motion is also represented at Figure 4.13. Average charge density is expressed as $\triangle\rho = \rho_{gr-100} - (\rho_{gr} + \rho_{100})$ where $\rho_{gr/100}$ is the charge density of whole structure with a 18.5 $\mathring{A}$ vacuum along z-direction, ρ_{100} is the charge density of Au(100) surface and ρ_{gr} is the charge density of graphene which is at 7.1 $\mathring{A}$ height above the bottom layer of Au(100). There is not a considerable variation is observed on average charge density, which gives the insight that friction force does not depend on the average charge of materials.

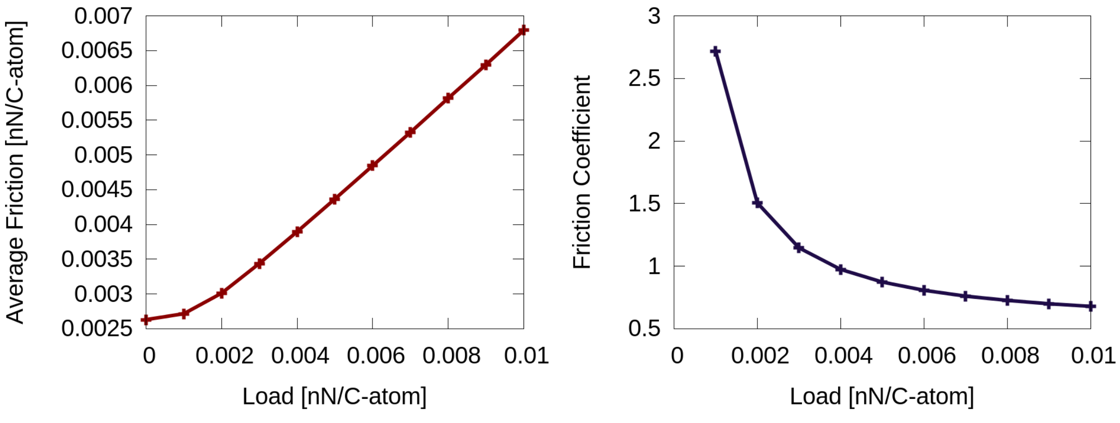

(a)

(b)

Figure 4.12: (a) Average lateral friction force (b)friction coefficient with increasing applied load over graphene-Au(100) interface configuration

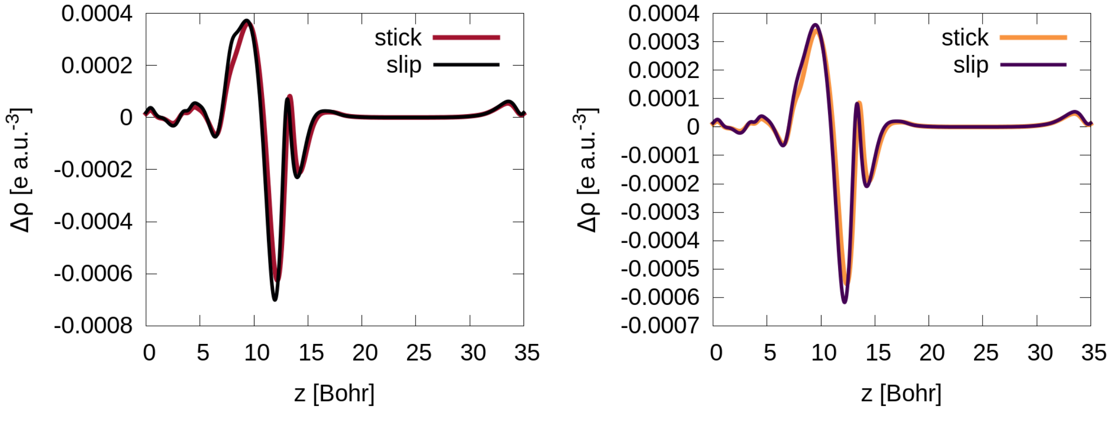

(a)

(b)

Figure 4.13: (a) Average charge density of stick-slip sites of graphene-Au(100) interface configuration under (a) 0 nN/C-atom (b) 0.005 nN/C-atom normal force

However, it may depend on the details of the charge distribution and further study is needed.

4.3.3.2 Au(110) Interface

As the applied vertical load on Au(110)-graphene configuration is increased, it is obtained that the interaction energy between surfaces also increases as seen at Figure 4.14(a). A comprehensible stick-slip behaviour in this configuration was not observed. One of the reason that could lead this kind of behaviour is the large unit cell of Au(110)-graphene structure along zigzag direction and while part of the atoms of surfaces were configured at on-top position other parts were at bridge or hollow sites during graphene surface is sliding. The collection of these interactions in different sites would give rise this kind of disrupted stick-slip motion. As a result of the lack of variation across different loads of the interaction energy profiles, the friction forces turn out to be identical for all loads as presented at Figure 4.14(b).

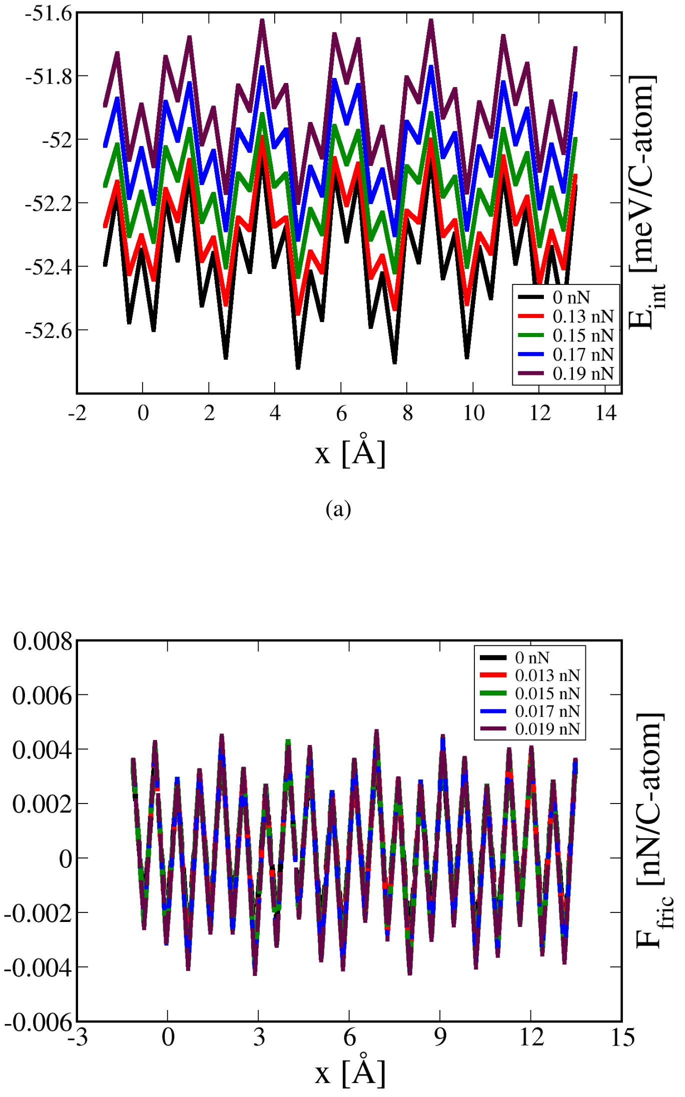

(a)

(b)

Figure 4.14: (a) Interaction energy (b) lateral friction force of vertically loaded Au(110)-graphene structure in several order of magnitudes

Table 4.6: Average friction force between Au(110) and graphene monolayer along x-direction with applied vertical contact force

F_{load} **[nN/C-atom]**	F_{avg} **[nN/C-atom]**
0	0.0028
0.005	0.0030
0.015	0.0032
0.017	0.0033
0.019	0.0034

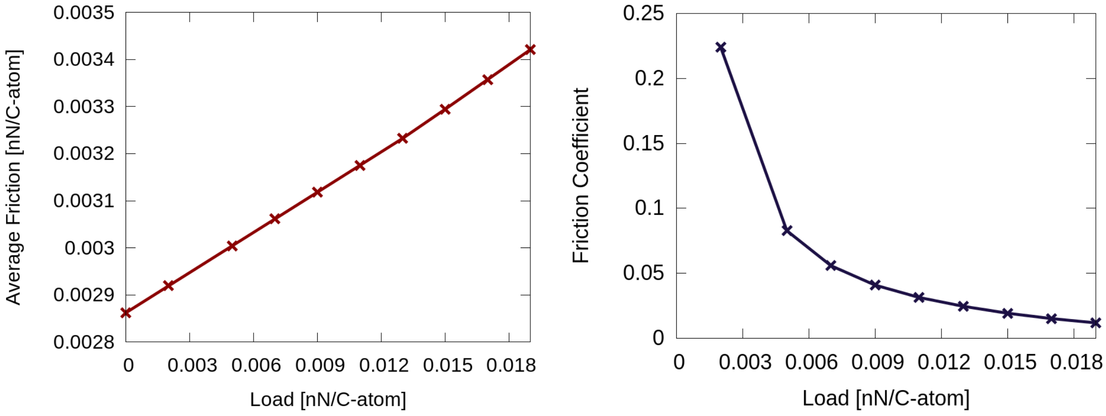

(a)

(b)

Figure 4.15: (a) Average lateral friction force (b)friction coefficient with increasing applied load over graphene-Au(110) interface configuration

The average friction force acting on the system under several magnitudes of normal load is presented in Table 4.6. It is observed that the friction force increases with applied load while friction coefficient follows a decreasing pattern as inversely proportional to the external normal load. The variation of F_{avg} and friction coefficient μ can be seen in Figure4.15.

The average charge density of the system under different loads by comparing the stick and slip positions of graphene is represented in Figure 4.16 and not a considerable variation is observed.

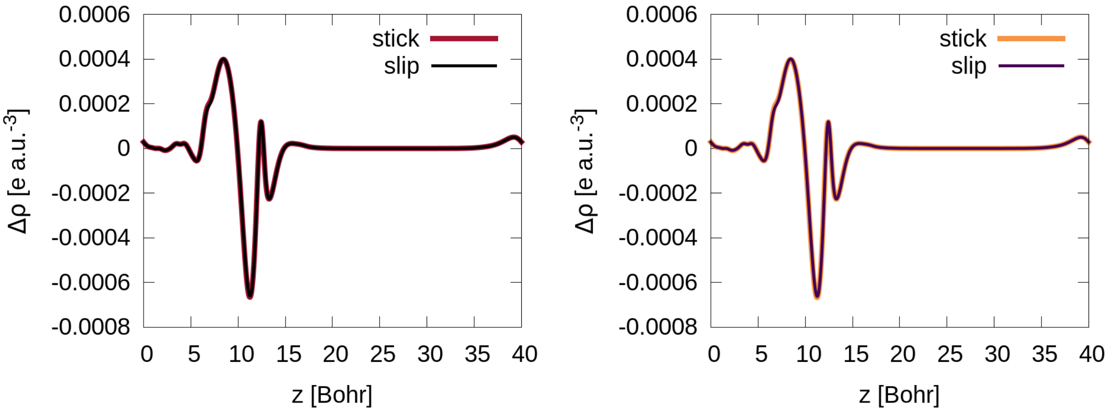

(a)

(b)

Figure 4.16: (a) Average charge density of stick-slip sites of graphene-Au(110) interface configuration under (a) 0 nN/C-atom (b) 0.019 nN/C-atom normal force

4.3.3.3 Au(111) Interface

For the Au(111) interface, an apparent stick-slip behaviour is not observed during sliding motion of graphene as shown at Figure 4.17(a). Since the Au(111) surface is the most dense configuration of fcc Au bulk structure, one reason of this behavior may be due to the multiple stick and slip occurrences concurrently. This feature of the structure leads the graphene lower stick events during the sliding part of motion after the graphene has passed over a potential barrier. The visualization of this stick-slip behaviour can be seen in Figure 4.17(b) in a comparative way in terms of normal load. The effect of normal load to interaction energy and friction of system is also presented in Figure 4.17(b) and 4.17(d).

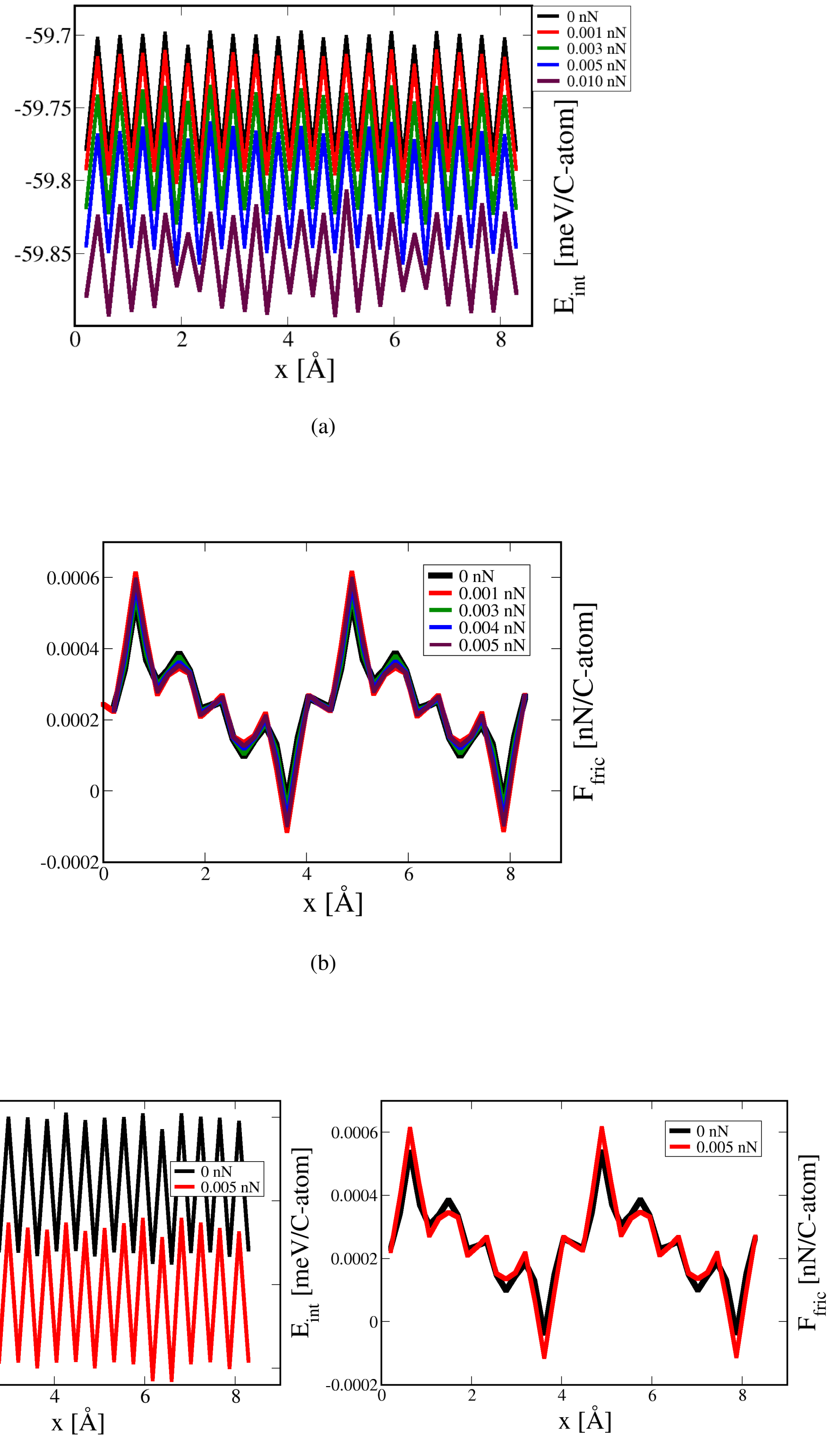

(a)

(b)

(c)

(d)

Figure 4.17: (a),(c) Interaction energy and (b),(d) lateral friction force of vertically loaded Au(111)-graphene structure in several order of magnitudes

Table 4.7: Average friction force between Au(111) and graphene monolayer along x-direction with applied vertical contact force

F_{load} **[nN/C-atom]**	F_{avg} **[nN/C-atom]**
0	0.000249
0.002	0.000251
0.004	0.000254
0.005	0.000255
0.010	0.000260

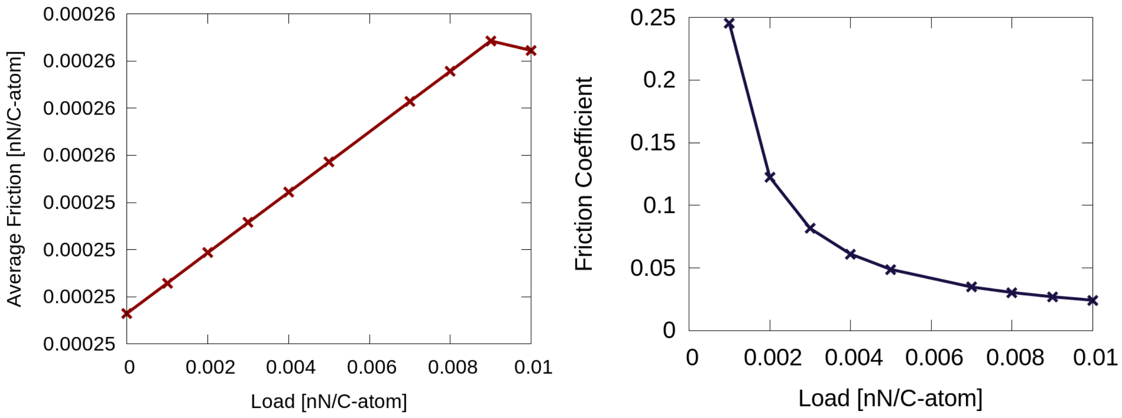

(a) (b)

Figure 4.18: (a) Average lateral friction force (b)friction coefficient with increasing applied load over graphene-Au(111) interface configuration

The average friction force acting on system and the friction coefficient between Au(111) and graphene layer can be seen at Figure 4.18. As the applied load gets larger, average friction shows an increasing trend proportional to load while μ decreases inversely proportional to applied load. The estimated values of F_{avg} are presented at Table 4.7

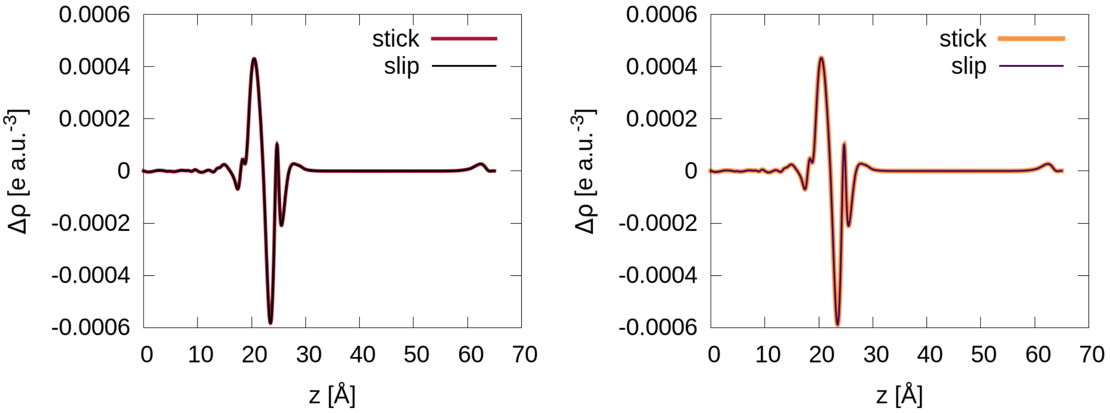

(a)

(b)

Figure 4.19: (a) Average charge density of stick-slip sites of graphene-Au(111) interface configuration under (a) 0 nN/C-atom (b) 0.005 nN/C-atom normal force

The average charge density of Au(111)-graphene system was also examined as shown in Figure 4.19. The results that shows no difference between stick and slip parts of the movement, also supports the idea that the effect of average charge density on friction behavior is inconsiderable.

CHAPTER 5

CONCLUSION

In this thesis we investigated the effects of applied normal load and layer thickness on the friction force at atomic scales by utilizing the density functional theory methodology. Our calculations focused on the interaction between graphene and three low dimensional Au surfaces namely Au(100), Au(110) and Au(111).

As a preliminary study, friction behaviour between graphene layers were examined as presented in Chapter 3. This benchmark calculations was conducted to identify a suitable protocol to express the vdW forces dominating the interaction between graphene layers and it was concluded that the vdW-DF2-C09 provides the most accurate results. The calculations achieved on bilayer and trilayer graphene structures revealed that the friction force acting on the structure increases almost linearly proportional to applied load while friction coefficient μ of interface decreases. It is also observed there is an inversely proportional relation between the friction and the number of layer as friction reduces in thinner systems [19]. Our results are also consistent with the previous first-principle study [56]

In Chapter 4 the friction force between graphene and Au surfaces was investigated. First of all, we obtained commensurate surfaces for graphene and Au interfaces by means of subjecting the surfaces to strains with slight percentage errors with respect to their original lattice parameters. After the equilibrium separation distance was obtained between graphene and each interface the lateral displacement of graphene was simulated over Au interfaces. In order to obtain the effect of normal load, interlayer separations of structures were manipulated. Throughout the sliding motion of graphene over the Au surfaces, several self-consistent DFT calculations were performed at each position along both lateral and vertical directions.

The most visible stick-slip behaviour was displayed at the graphene/Au(100) interface. The applied external load leads to a significant difference in amplitude of the interaction energy and as a consequence of this behaviour the friction force required to pass over an energy barrier increases with load. Again, it is concluded that the friction force sublinearly increases while friction coefficient decreases as the normal load increase for this structure.

The normal force did not lead to a significant difference in the amplitude of potential barrier for graphene/Au(110) structure except for a slight increase. The stick-slip behavior of friction was not clearly observed at this configuration due to the large simulation cell size along the sliding path and large number of atoms involving the interaction. In this structure it was obtained that the average friction increases proportional to applied load while friction coefficient decreases inversely proportional to it.

For the graphene/Au(111) configuration, the variation of interaction energy showed a similar behavior to Au(110) system at different values of normal load. However, for this structure the stick-slip nature of friction was observed more explicitly with the smaller orders of several stick behaviours during sliding of surface. The reason behind this presence of stick is the dense configuration of Au(111) surface where several potential wells occur as the graphene layer changes its position. Thus, the force that is required for the layer to pass over a high potential well is so large that it leads a several jumps over smaller potentials, too. This configuration gives rise to large incommensurability, thereby providing lowest interaction force. For this system, it is also obtained that the friction force increases while the friction coefficient decreases as the normal load increases.

With the attempt to investigate the mechanism behind friction between surfaces, average charge density of each system was also analysed by comparing the zero load and applied normal load conditions. However, not a significant difference was observed in average charge density and transfer between surfaces. This result is consistent with the previous study of Wang et. al. with the proposal of the key reason behind friction and potential corrugation is the charge density fluctuation rather than average charge density.

REFERENCES

[1] Cahangirov S., Ataca C., Topsakal M., Sahin H., and Ciraci S. Frictional figures of merit for single layered nanostructures. *Phys. Rev. Lett.*, 108:126103, (2012).

[2] Gnecco E., Bennewitz R., Gyalog T., C. Loppacher, M. Bammerlin, E. Meyer, and H.J Guntherodt. Velocity dependence of atomic friction. *Phys. Rev. Lett.*, 84:1172–1175, (2000).

[3] B. Bhushan. *Introduction to Tribology*. Wiley, New York, (2013).

[4] Mate C. M., Mcclelland G. M., Erlandsson R., and Chiang S. Atomic-scale friction of a tungsten tip on a graphite surface. *Phys. Rev. Lett*, 59:1942–1945, (1987).

[5] Ebru Cihan. Structure and nanotribology of thermally deposited gold nanoparticles on graphite. Master's thesis, Bilkent University, 2015.

[6] Prandtl L. Hypothetical model for the kinetic theory of solid bodies. *Z. Angew. Math. Mech.*, 8:85–106, (1928).

[7] Tomlinson G. A molecular theory of friction. *Philos. Mag.*, 7:905, (1929).

[8] Kontorova T. and Frenkel Y. I. On the theory of plastic deformation. *Zh. Exp. Teor. Fiz*, 8:1340–1344, (1938).

[9] Feeny B., Guran A., and Hinrichs N.and Popp K. A historical review on dry friction and stick-slip phenomena. *Appl. Mech. Rev*, 51:321–341, (1998).

[10] Mang T., Bobzin K., and Bartels T. *Industrial Tribology: Tribosystems, Friction, Wear and Surface Engineering, Lubrication*. Wiley-VCH, (2011).

[11] Amontons G. De la resistance caus' ee dans les machines. *Mémoires de l'Académie Royale*, page 257–282, (1706).

[12] Dowson D. *History of Tribology*. Longman, second edition, (1998).

[13] Bowden F.P. and D. Tabor. *The Friction and Lubrication of Solids*, volume 13. Clarendon, Oxford, (1950).

[14] Müser H. M. The velocity dependence of kinetic friction in the prandtl-tomlinson model. *Phys. Rev. B*, 84:125419, (2011).

[15] Popov V. L. and Gray J.A.T. Prandtl-tomlinson model: History and applications in friction, plasticity, and nanotechnologies. *Z. Angew. Math. Mech.*, 92:683–708, (2012).

[16] Krylov Yu. S. and Frenken J. W. M. The physics of atomic-scale friction: Basic considerations and open questions. *Phys. Status Solidi*, 251:711–736, (2014).

[17] Bouhacina T. Aimé J. P., Gauthier S., Michel D., and V. Herogue V. Tribological behavior of a polymer grafted on silanized silica probed with a nanotip. *Phys. Rev. B*, 56:7694, (1997).

[18] Zhong W. and Tomanek D. First-principles theory of atomic-scale friction. *Phys. Rev. Lett*, 64:3054–3057, (1990).

[19] Lee C.G., Li Q. Y., Kalb W., Liu X. Z., Berger H., and Carpick R. W. Frictional characteristics of atomically thin sheets. *Science*, 76:328, (2010).

[20] Nian J., Si Y., and Guo Z. Advances in atomic-scale tribological mechanisms of solid interfaces. *Tribology International*, 94:1–13, (2016).

[21] Reguzzoni M., Fasolino A., Molinari E., and Righi M. C. Friction by shear deformations in multilayer graphene. *J. Phys. Chem. C*, 116:21104–21108, (2012).

[22] Cahangirov S., Çıracı S., and Özçelik V. O. Superlubricity through graphene multi-layers between ni(111) surfaces. *Phys. Rev. B*, 87:205428, (2013).

[23] Filleter T., McChesney J. L., BostwickA., Rotenberg E., Emtsev K. V., Seyller Th., Horn K., and Bennewitz R. Friction and dissipation in epitaxial graphene films. *Phys. Rev. Lett.*, 102:086102, (2009).

[24] Klemenz A., Pastwka L., Balakrishna S. G., Caron A., Bennewitz R., and Moseler M. Atomic scale mechanisms of friction reduction and wear protection by graphene. *Nano Lett.*, 14:7145–7152, (2014).

[25] Cahangirov S., Ataca C. Topsakal M., Sahin H., and Ciraci S. Frictional figures of merit for single layered nanostructures. *Phys. Rev. Lett.*, 108:126103, (2012).

[26] Wang L., Zhou X., Ma T., Liu D., Gao L., Li X., Zhang J., Hu Y., Wang H., Dai Y., and Luo J. Superlubricity of a graphene/mos2 heterostructure: a combined experimental and dft study. *Nanoscale*, 9:10846–10853, (2017).

[27] Wolloch M., Feldbauer G., Mohn P., Redinger J., and Vernes A. Ab initio friction forces on the nanoscale: A density functional theory study of fcc cu(111). *Phys. Rev. B*, 90:195418, (2014).

[28] Gosvami N., Filleter T., Egberts P., and Bennewitz R. Microscopic friction studies on metal surfaces. *Tribol. Lett.*, 39:19, (2010).

[29] Born M. and Oppenheimer R. Zur quantentheorie der molekeln. *Ann. Phys.*, 84:457, (1927).

[30] Kohn W. Nobel lecture: Electronic structure of matter—wave functions and density functionals. *Rev. Mod. Phys.*, 71:1253, 1999.

[31] Perdew P., Burke K., and Ernzerhof M. Generalized gradient approximation made simple. *Phys. Rev. Lett.*, 77:3865–3868, (1996).

[32] Hohenberg W. and Kohn W. Inhomogeneous electron gas. *Phys. Rev.*, 136:864, (1964).

[33] Dobson J. F., Vignale G., and Mukunda P. D. *Electronic Density Functional Theory recent progress and new directions*. Springer, (1996).

[34] Kohn W. and Sham L.J. Self-consistent equations including exchange and correlation effects. *Phys. Rev.*, 140:1133, (1965).

[35] Vanderbilt D. Soft self-consistent pseudopotentials in a generalized eigenvalue formalism. *Phys. Rev. B.*, 7892:41, (1990).

[36] Grimme S., Antony J., Ehrlich S., and Krieg H. A consistent and accurate ab initio parametrization of density functional dispersion correction (dft-d) for the 94 elements h-pu. *J. Chem. Phys.*, 132:154104, (2010).

[37] DiLabio G. A. and Otero de-la Roza A. Noncovalent interactions in density-functional theory. *Phys. Chem.-ph*, arXiv:1405–1771, (2014).

[38] Lundqvist B. I., Andersso Y., Shao H., Chan S., and Langreth D. C. Density functional theory including van der waals forces. *International Journal of Quantum Chemistry*, 56:247–255, (1995).

[39] Zhang Y. and Yang W. Comment on “generalized gradient approximation made simple". *Phys. Rev. Lett*, 80:890, (1998).

[40] Perdew C. P. and Wang Y. Accurate and simple density functional for the electronic exchange energy: Generalized gradient approximation. *Phys. Rev. B*, 33:8800, (1986).

[41] Cooper V. Van der waals density functional: An appropriate exchange functional. *Phs. Rev. B*, 81:161104, (2010).

[42] Hamada I. and Otani M. Comparative van der waals density-functional study of graphene on metal surfaces. *Phys. Rev. B.*, 82:153412, (2010).

[43] P. Giannozzi et al. Quantum espresso: a modular and open-source software project for quantum simulations of materials. *J. Phys.:Condens. Matter*, 21:395502, (2009).

[44] Monkhorst H.J. and Pack J. D. Special points for brillouin-zone integrations. *Phys. Rev. B.*, 13:5188–5192, (1976).

[45] Feynman R.P. Forces in molecules. *Phys. Rev.*, 56:340, (1959).

[46] Hellman H. *Einführung in die Quantenchemie*. Springer, (1937).

[47] Burke K., Perdew P., and Wang Y. *Derivation of a generalized gradient approximation: The PW91 density functional*. Plenum, (1997).

[48] Perdew P. and Zunger A. Self-interaction correction to density-functional approximations for many-electron systems. *Phys. Rev. B.*, 23:5048, (1981).

[49] Baskın V. and Meyer L. Lattice constants of graphite at low temperatures. *Phys. Rev.*, 100:544, (1955).

[50] Lebadeva V., Knizhnik A., Popov M., Lozovik E., and Potapkin V. Interlayer interaction and relative vibrations of bilayer graphene. *Phys. Chem. Chem. Phys.*, 13:5687–5695, (2011).

[51] Reguzzoni M., Fasolino A., Molinari E., and Righi M.C. Potential energy surface for graphene on graphene: Ab initio derivation, analytical description, and microscopic interpretation. *Phys. Rev. B.*, 86:245434, 2012.

[52] Ye Z., Tang C., and Dong Y. Role of wrinkle height in friction variation with number of graphene layers. *Journal of Applied Physics*, 112:110–113, (2012).

[53] Mo Y., Turner K., and Szlufarska I. Friction laws at the nanoscale. *Nature*, 457:1116–1119, (2009).

[54] Marchetto D., Feser T., and Martin Dienwiebel M. Microscale study of frictional properties of graphene in ultra high vacuum. *Friction*, 3:161, 2015.

[55] De Graef M. and McHenry M. E. *Structure of Materials: An Introduction to Crystallography, Diffraction and Symmetry*. Cambridge University Press, (2007).

[56] Zhuang C. and Liu L. Atomic-scale friction behavior of layered graphene and graphene-like bn materials modulated by interaction potential. *AIP Advances*, 7:085103, (2017).